A COMPUTATIONAL STUDY OF

INDUCTION STIRRED LADLES

A Thesis

Submitted to the Faculty

of

Purdue University

by

Joshua D. Vandenoever

In Partial Fulfillment of the

Requirements for the Degree

of

Master of Science in Mechanical Engineering

December 2019

Purdue University

Hammond, Indiana

THE PURDUE UNIVERSITY GRADUATE SCHOOL
STATEMENT OF THESIS APPROVAL

Dr. Chenn Zhou, Chair

    Department of Mechanical and Civil Engineering

Dr. Harvey Abramowitz

    Department of Mechanical and Civil Engineering

Dr. Xiuling Wang

    Department of Mechanical and Civil Engineering

Approved by:

    Dr. Chenn Zhou

        Head of the School Graduate Program

To my Father

ACKNOWLEDGMENTS

I would like to thank Professor Chenn Zhou for opportunities provided to me while researching at the Center for Innovation through Visualization and Simulation (CIVS). I was granted the responsibility of developing the electromagnetic and magnetohydrodynamic numerical simulations, which are two areas of deep interest of mine. I am also very thankful for the aid provided by the staff at the CIVS research center. Additionally, I would like to thank Dr. Rui Liu for his support and advice throughout the development of the numerical models.

I am acknowledging and thanking the authors Qing Cao and Laurentiu Nastac [1] for their depiction and choice of colors for clearly describing the behavior of the ladle interior. I attempted using other color combinations which resulted in less aesthetically pleasing renditions. Fig. (1.2) and Fig. (1.3) are based on their original images.

I am grateful for my upbringing guided by my parents. My father and mother, David and Carrie Vandenoever, have always pushed me to exhibit diligence in all of my work. They have always supported me throughout the several years of my determination and hard work which has brought me this far.

Lastly, I would like to thank my girlfriend, Andie Wahlberg. I thank you for your continuous support, understanding, and patience throughout this rigid course. I am forever grateful for the time and detail you have spent during the proofreading process. You have continually been a place of comfort and joy in my life, I thank you so much for that.

TABLE OF CONTENTS

LIST OF TABLES

LIST OF FIGURES

SYMBOLS

A	General wave amplitude
$\vec{B}$	Magnetic field [T]
$\vec{E}$	Electric field [V/m]
f	Frequency [Hz]
$\vec{F}_C$	Coulomb force [N]
$\vec{F}_L$	Lorentz force [N]
$\vec{F}_V$	Volumetric Lorentz force [N]
I	Electric current [A]
$\vec{J}$	Electric current density [A/m^2]
j	Imaginary number
k	Wave number [Rad/m]
l_c	Characteristic length scale [m]
m	Mass [kg]
q	Electric charge of a charged particle [C]
Q	Total electric charge [C]
R_m	Magnetic Reynolds number
S_f	Scaling factor
S_{M_i}	Momentum source term per coordinate index i [kg·m/s]
S_ϕ	General source term
$\vec{v}_c$	Charged particle velocity [m/s]
$\vec{V}$	Velocity vector [m/s]
u, v, w	Velocity per Cartesian coordinate (x, y, and z) [m/s]
α	Electromagnetic wave attenuation constant
δ_s	Skin depth [m]

Δt	Timestep [s]
Δx	Grid length [cm]
ϵ	Electric permittivity [F/m]
ϵ_o	Electric permittivity of free space [F/m]
ϵ_r	Relative electric permittivity
ϵ'	Real component of electric permittivity [F/m]
ϵ''	Imaginary component of electric permittivity [F/m]
$\mathcal{E}$	Electromagnetic force [V]
λ	Wavelength [m]
λ_B	Magnetic diffusivity [m^2/s]
μ	Magnetic permeability [H/m]
μ_o	Magnetic permeability of free space [H/m]
μ_r	Relative magnetic permeability
ρ_e	Electric charge density [C/m^3]
ρ	Density [kg/m^3]
σ	Electrical conductivity [S/m]
τ	Magnetic damping time [s]
ϕ_s	Phase shift [Degree or Rad]
Φ_B	Magnetic field flux [Wb]
Φ_E	Electric field flux [V·m]
Ψ	General wave function
ω	Angular frequency [Rad/s]
∇	Del operator
$\otimes$	Magnetic field vector directed into the plane
$\odot$	Magnetic field vector directed out of the plane

ABBREVIATIONS

AC	Alternating Current
EMF	Electromotive Force
EMGAS	Combined Electromagnetic/Gas stirring
EMS	Electromagnetic Stirring
FDM	Finite Difference Method
FEM	Finite Element Method
FVM	Finite Volume Method
LF-EMS	Low Frequency Electromagnetic Stirring
MHD	Magnetohydrodynamics
TMF	Traveling Magnetic Field
UDF	User-Defined Function

ABSTRACT

Vandenoever, Joshua D. M.S.M.E, Purdue University, December 2019. A Computational Study of Induction Stirred Ladles. Major Professor: Chenn Zhou.

A numerical simulation was developed to capture the phenomena of electromagnetic stirring in a metallurgical ladle. Electromagnetic stirring requires an external magnetic field to be imposed on the molten steel bath, which is governed by the principles of magnetohydrodynamics. Electromagnetic stirring benefits over traditional stirring methods by offering non-invasive stirring, melt homogeneity, and ease of configuration alterations. Insight to the electromagnetic stirring phenomena is limited experimentally due to the high temperatures of the molten-steel bath. This investigation will include two numerical simulations, the first of which is to generate a magnetic field to properly stir the steel bath. The second incorporates the generated magnetic field and solves the fluid flow due to the magnetohydrodynamics interactions. The results of these numerical simulations will help to provide further understanding of the electromagnetic stirring method. This simulation was used to analyze the molten-steel bulk velocity, vortex formation, flow development time, slag-eye size, and wall shear stress in a metallurgical ladle.

The transient development of the bulk velocity in an EMS ladle was compared with the literature study completed by Sand et al. 2009. The comparison of the developed bulk velocity resulted in a percentage difference of 0.98% and an absolute difference of 0.007 [m/s]. Both numerical models, in the current work and the literature study, obtained a developed flow within 25 seconds of stirring. For the parametric studies, it was found that the addition of a circumferential taper angle to the geometry reduced the bulk velocity and slag-eye size formed compared to a cylindrical ladle. The electric current amperage of the external magnetic field coil

system was determined to precisely adjust the bulk velocity. A 150 [A] reduction in amperage results in a $\sim 20\%$ loss in the bulk velocity magnitude. The locations of the high shear stress regions were determined which remained near the stirring unit. From this study, it is recommended to use a magnetohydrodynamics package offered within a multiphysics numerical solver since the FLUENT® MHD module inherently under-predicts the velocity as well as the issue of the numerical instabilities of the Lorentz force calculations.

1. INTRODUCTION

1.1 Background

Ladle refining is a crucial step in the steelmaking process. The ladle is purposed for mixing the molten steel bath, obtaining temperature homogeneity, purifying steel, and adjusting the alloy composition. The quality of the steel ensures the integrity of the machines and equipment created from steel. Therefore, reducing possible impurities in the final product is a common goal among steel manufacturer's, which is considered during the steel refinement within ladles.
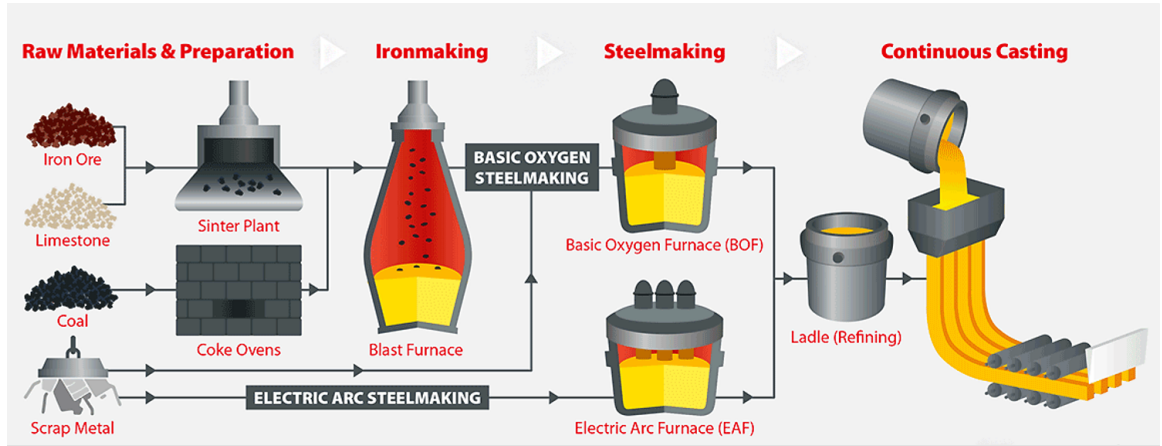
Fig. 1.1: Steel production process [2].

Major steel production processes either fall under the primary or secondary stages, Fig. (1.1). The primary steelmaking stage combines liquid iron and molten scrap to form crude steel. The melt down process, which varies per method, either occurs in a blast furnace or an electric arc furnace. The secondary steelmaking stage is focused on steel refinement. This is generally controlled with batches of molten steel contained in ladles. There are three types of ladles: transfer, treatment (or refining), and casting

ladles. The transfer ladle transports molten steel from the primary stage furnaces to the other treatment processes. The treatment ladle is focused on stirring the molten bath allowing for alloy additives and removal of impurities obtained from crude steel and oxidation. These impurities are known as inclusions. Lastly, the casting ladle pours refined steel into an intermediate container called the tundish before entering the casting stage. The tundish allows for smooth transition between the ladle and the caster. The casting process is where molten steel is poured into a mold where it is cooled and formed into steel slabs or other forms. The caster has primary and secondary cooling stages with conductive and liquid spray coolers, respectively. The steel is solidified between rollers and transferred out to the rolling mills.

1.1.1 Ladle Stirring Methods

Steel industry ladle capacity ranges between 100-300 tons which needs to be processed and maintained through the refinement processes. The main stages for the ladle refinement are heating, degassing, and alloy addition [3]. The efficiency of all three are dependent on the stirring of the melt. The refining ladle has two major stirring methods: gas injection and electromagnetic stirring (EMS). Combined electromagnetic and gas stirring (EMGAS) is another method implemented in industry and research studies, but this work concerns itself solely with the flow characteristics of EMS. Several factors have to be considered before choosing one of these stirring methods. First is the timeline of equipment development. The induction stirrer began taking effect in the 1980's [3], however gas injection has been around for the last 150 years [4]. More is known about the gas stirring method since the gas stirring has been around longer, which makes this process a more common method in steelmaking. The gas stirring has more mechanisms for inclusion removal but a limited flow field whereas the EMS flow field is free of dead zones but less inclusion removal mechanisms. EMGAS has been found to create high shear stress regions on the la-

dle refractory wall that decreases the lifetime of the ladle. In any case, the mixing methods have six key factors [5] to take into account, listed below.

Factor 1: Cleanliness

Factor 2: Chemistry and Temperature Control

Factor 3: Reproducibility

Factor 4: Reliability industry/collaborator

Factor 5: Safety

Factor 6: Cost of Operation

Each item listed will be discussed further in the following two sections. First for how these pertain to gas stirring, then for EMS.

1.1.2 Gas Stirring

Gas stirring is obtained by injecting argon bubbles into a refining ladle. This typically is accomplished by a porous plug in the bottom of the ladle. The ladle is not limited to one plug, it can have multiple injection ports using different geometries. The positions effect the flow development, wall shear stress, and overall operation of the ladle, especially when different flow rates are taken into consideration. For simplicity, a depiction of a single bottom plug injection ladle is shown in Fig. (1.2), which includes the three phases within the ladle (steel, argon, and slag) and a drastically simplified count of inclusions. **Factor 1** is focused on the removal of inclusions. During the stirring process, inclusions can be removed by three mechanisms: slag removal, wall removal, and bubble transport [6]. Slag and wall removal rely on the interaction and attachment of inclusions. The argon bubbles are injected from the bottom and will travel up though the slag layer, due to the injection flow rate and density differences. During this transit, the bubbles will expand into a plume distribution where the bubbles will break apart and coalesce. This adds complexity into the bubble removal since it relies on the bubble and inclusion remaining attached

throughout the transit. Inclusions can reenter the steel after a successful bubble attachment during bubble breakup, collision, and impact at the slag layer.
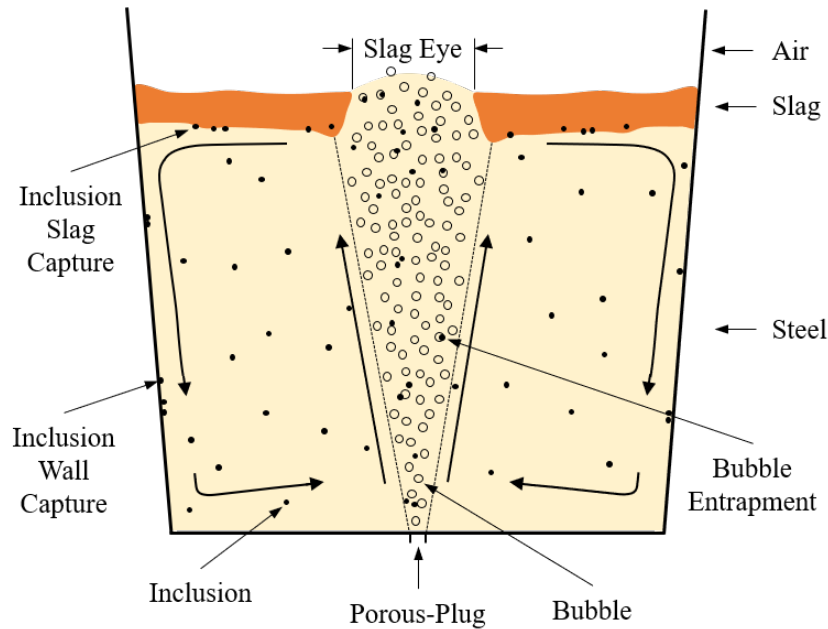
Fig. 1.2: Bottom plug gas injection ladle.

Factor 2 is maintained within a gas stirred ladle through the developed flow field. A negative aspect of the gas flow field is the dead-zones that are formed near the bottom edges and surrounding the plume area, which inhibits temperature homogeneity. The plume head is centralized above the injection port, creating a turbulent steel-slag interface which is crucial for de-sulphurization within the ladle [7]. **Factor 3** is important to maintain steel quality across production timelines. Gas stirred ladles face the issue of injection port plugging. This occurs when sculls form within the ladle and block the injection port, or can also occur with poor injection port maintenance. A blocked injection port would stop the argon flow into the steel, stopping the stirring process. These issues impact all six factors. This would impact the quality of the steel since the stirring would cease, or at least be reduced in a multiple plug setup. The solution for a blockage occurrence requires personnel to notice the issue and to set up a backup system, either a secondary plug or lance. A lance is lowered into the steel and argon bubbles are injected into the steel through the lance port. Setting up

either backup system will yield a longer stirring time that will introduce more wear on the ladle, irregular operating conditions, and longer heating times resulting higher costs.

1.1.3 Induction Stirrers

Magnetic fields are utilized in several processes within the metallurgical industry including stirring, braking, pumping, levitating, and heating of liquid steel [3]. EMS works on the basis of Magnetohydrodynamics (MHD). MHD governs the interactions between magnetic field and a conductive fluid, see §2.3. Low-frequency (LF) EMS systems are comprised of an EMS unit, frequency converter, a transformer, and water cooling station. A requirement for the ladle wall facing the stirrer is to be non-magnetic stainless steel so that the magnetic field can penetrate through the wall [7].

For the EMS ladle, two stirrer options are available: straight or cylindrical. A cross-section of a straight stirrer next to a ladle is depicted in Fig. (1.3). A cylindrical stirrer completely surrounds the exterior of the ladle. The straight stirrer coil system benefits from simple implementation. A straight stirrer needs to be set near a ladle, whereas the cylindrical coil system would require the ladle to be lowered within the coils. More importantly, in the case of a ladle wall breakout, the straight stirrer could be removed easily [3]. In either case, the magnetic field induced from the coil system must be an AC field. These coil systems can produce useful stirring field types of polyphase rotating magnetic fields, helicoidal magnetic fields, traveling magnetic fields (TMF), that operate at LF [8]. All fields produce a flow field that is driven by a large fluid eddy current. The difference is the orientation and complexity of the flow field. The flow field shown in Fig. (1.3) is the result of a straight stirrer with a TMF. The flow is counter-clockwise, in reference to the cross-section plane, which depends on the stirring unit direction setting. Straight TMF stirrers can be directed for upward (clockwise flow field) or downward (counter-clockwise flow field) stirring.

The rotating or helicoidal field will produce an azimuthal flow field in reference to the cross-section plane in Fig. (1.3).
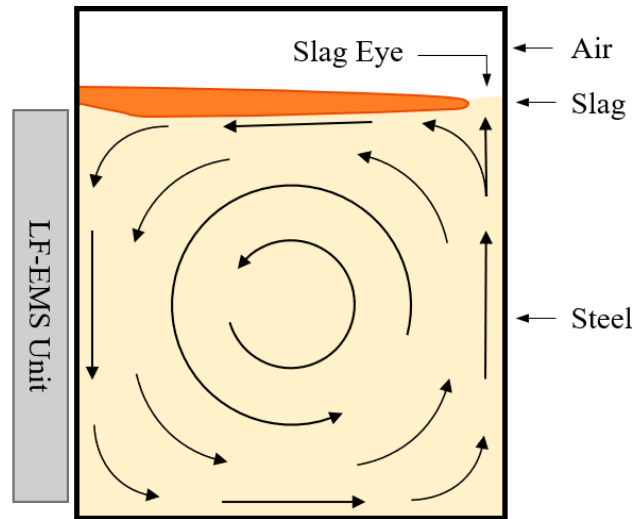
Fig. 1.3: Downwar stirring EMS ladle.

Factor 1 in an EMS ladle is obtained by two of the three inclusion removal mechanisms discussed in §1.1.2. These mechanism are wall and slag removal. Since there are no bubbles to capture and transport inclusions, the removal is reliant on the flow field pushing the inclusions to the wall and slag surfaces. Slag eye development can be reduced or completely avoided with EMS since the flow field is primarily tangential to the slag surface, while maintaining a strong stirring. The slag eye may be opened to introduce alloy additives or closed to ensure oxidation reduction by varying the amperage of the induction coils [5]. This is accomplished by increasing or decreasing current amperage within the induction coils [7]. Note that there are no slag-eyes through the primary EMS process. For **Factor 2**, unlike gas injection, no dead-zones are formed with EMS. The vortex formed in the center of the melt will drive the flow, distributing temperature and chemistry better than gas stirring. **Factor 3** and **Factor 4** are highly improved by negating the concern of injection port clogging and the precision of flow field variations due to current amperage adjustments. **Factor 5** is increased through the noninvasive stirring, whereas weak points are created with the gas stirred ladle by the injection port that penetrates the refractory lining. For

Factor 6, a cost analysis between a 130 ton EMS and gas stirred ladle was conducted by the company ABB [5]. It was reported that an hour treatment time in both stirring methods results in gas stirring costing 148,205 USD/year more than EMS.

1.2 Literature Review

This literature review begins with a qualitative description of the MHD involved for this project. It then explains various methods of obtaining the numerical magnetic field source. Lastly, it provides details on how these methods have been used in other literature studies.

1.2.1 Defining the System

The analysis of MHD falls within two regions, uncoupled and coupled, which drastically impacts the complexities of the system, [9]. The fine details of where the system lies will be further discussed in §2.3. Large scale metallurgy EMS ladles tend to fall on a fine line of being coupled, increasing the complexity of calculating the flow regime. For this reason, most research in this area are conducted numerically. There are preferred methods of numerical modeling of MHD to overcome its complexity, but this project will focus on the least computationally preferred method.

1.2.2 Numerical Methods of Obtaining a Magnetic Field Source

There are five major steps for solving the MHD phenomena with an 'uncoupled' simulation process: first is obtain a source of the external transient magnetic field; second is to build the geometry and mesh; third is to determine the boundary conditions involved in the fluid domain; fourth is to apply a magnetic field source to the fluid domain; last is to solve the governing equations through a selected computational fluid dynamics (CFD) software. This process will change depending on the

origin of the magnetic field source. There are also five common methods found in literature ([10], [11], and [3]) for obtaining the magnetic field source:

Method 1: Simulate the external magnetic field

Method 2: Obtain the external magnetic field from industry/collaborator

Method 3: Obtain Lorentz force distribution data from the simulated magnetic field

Method 4: Obtain the Lorentz force distribution data from industry/collaborator

Method 5: Pair Lorentz force data with time-dependent semi-empirical formulas

Method 1 requires a finite element method (FEM) simulation of the induction coils to be created to obtain the external magnetic field that will be imposed in the fluid domain. This benefits from having the true description of the magnetic field impacting the fluid, and it provides the transient development of the flow field. On the negative side, this method requires the MHD governing equations to be solved which tends to have convergence instabilities and numerical complexities, as well as the need for validation of the FEM simulation. **Method 2** evades the FEM simulation and validation of the induction coil setup. It only concerns itself with the magnetic field data as source terms in solving the MHD equations, which still has the computational difficulties. **Method 3** requires simulating the magnetic field penetrating the conductive fluid that will be used in the CFD simulation. The Lorentz force distribution formed in this simulation will then be extracted and used in the CFD simulation as momentum source terms. This will only produce the steady-state results of the flow field. The benefit is circumventing the computational costs and strain of solving the MHD equations, but lacks in insight to the transient development. This method, like **Method 1** will need validation of the magnetic field simulation. **Method 4** is desirable since it is a simple implementation and the field is true to the physical induction coil system. A variant of this method is **Method 5** which updates the forces in the major stirring directions. This requires the Lorentz force distribution to be obtained and time-dependent semi-empirical formula(s) will have to be derived for the geometry, boundary conditions, and properly express the influence of the basis

magnetic field. This will provide the transient flow development and benefit from less computational expenses faced by **Method 1** or **Method 2**. Note, **Method 3**–**Method 5** are largely approximations of a transient magnetic field which can not fully describe the MHD interactions. In any case, the magnetic field source data will be extracted from a separate simulation and imported into the CFD simulation.

The previous methods (**Method 1**–**Method 5**) pertained to a work flow process of magnetic field generation in an electromagnetic software then importing the magnetic field into a separate fluid dynamics solver. Another method that can be implemented is solved using a multiphysics solver. This negates the magnetic field data source export/import process. This allows for the external magnetic field and fluid interactions to be solved at the same time.

1.2.3 Implementation of the Numerical Magnetic Field Sources

For simplicity sake, utilizing the 'frozen' Lorentz force distribution is commonly used. As mentioned before, adding time-dependent semi-empirical expressions allow for a transient simulation. This method was implemented by Sand et al. [10] in 2009 for their evaluation of the EMS ladle with a straight stirrer using ANSYS FLUENT®. Their analysis consisted of a simplified cylindrical ~130 ton ladle. This included the two-phase flow interaction between the steel bath and slag layer, which was governed by the Volume of Fluid (VOF) method. The k-ϵ model was selected to govern the turbulence. They validated the simulated results through water modeling. The Lorentz force distribution was extracted from an unnamed commercial software, and they utilized **Method 5** with a single empirical formula to update the vertical stirring force. It was determined that upward and downward stirring produced a volume-averaged velocity of 0.5 [m/s] and 0.7 [m/s], respectively. The slag-eye developed on the opposing side of the EMS unit. The mixing time was monitored by placing pre-defined points within the steel phase. The mixing time was determined once a 5% difference

was obtained between the mean concentration and the calculated values. This study was completed by the company ABB that produces the EMS units.

Method 1 was compared against **Method 5** by Javurek et al. [11] in 2008 to investigate solidification in the continuous caster. Again, the basis magnetic field was provided by ABB. This magnetic field had a frequency of 2.5 [Hz]. ANSYS FLUENT® was selected as the CFD solver. They implemented semi-empirical formulas that governed the radial and tangential stirring forces. The FLUENT® MHD module was found to produce induced magnetic fields that were not divergence free (see §2.3.2). The turbulence model selected was the realizable k-ϵ. They tested the stability of the FLUENT® MHD module. It was found that the FLUENT® MHD module required a timestep, Δt, much smaller than the period of the magnetic field supplied. The numerical stability also required that the inner-iterations should run up to $\sim$300 iterations. The boundary conditions selected for the FLUENT® MHD module assumed that all magnetic field lines leave normal to the boundary. FLUENT® labels this condition as an "insulating boundary". They determined that the FLUENT® MHD module resulted in force deviations of $\pm 40\%$. The conclusion was that the force density method benefits from simple implementation but the solution has questionable accuracy due to the approximations of the semi-empirical formulas. Also, the FLUENT® MHD module is unacceptably computationally expensive due to low convergence of the induction equations.

A multiphysics simulation was completed by Pal et al. [3] in 2012 which covers metallurgical EMS simulations along with an explanation of fundamental heat transfer considerations. The numerical solver used was COMSOL Multiphysics®. A straight stirrer EMS unit was the focus of this work. The computational domain contained both the stirring unit and the fluid domain. The k-ϵ model was used for turbulence modeling. The boundaries had to be significantly larger than the two components to properly solve for the electromagnetic fields. The CFD aspect governed a single phase (steel) mixing problem where the transport equations were assumed to be in steady-state. The multiphysics simulation solved for the Lorentz forces within the

melt then applied them as momentum source terms (**Method 5**). Validation of the flow velocity was determined within 8%. The magnetic field was validated with experimental results.

All other works presented have been isothermal studies. A main characteristic of AC driven magnetic fields is the effect of Joule heating. This was accounted for in a 2016 study conducted by Fireteanu et al. [8]. This study is focused on the MHD interactions of a small scale molten glass bath. They also used ANSYS FLUENT® MHD module through **Method 3**. It introduces the impact of monophase and several polyphase induction coil systems. The coil systems were setup for a TMF, rotating, and helicoidal magnetic fields. This study gave insight to the relation phase shifts to create a TMF. It specifies that the magnetic field were low frequency, polyphase AC fields, which produced high magnitude Lorentz forces.

1.3 Objectives

The primary objective of this project is to develop an isothermal, transient, three-dimensional numerical model of an electromagnetically stirred ladle. This requires two primary simulations. The first simulation will govern the induction coils that generate the external magnetic field. The other simulation will use the generated magnetic field to simulate the magnetohydrodynamic interactions between a molten steel bath and the external magnetic field. These simulations will provide insight to the flow field development, mixing time required to obtain quasi-equilibrium, and mixing speed of the molten bath. Once the developed bulk motion velocity and time are compared to literature results, the simulations may be used for further studies. The extended studies will include comparisons on electric current amplitude, ladle geometry, slag-eye formation, and wall shear stress.

2. THEORY AND NUMERICAL METHODS

As discussed in §1.3, the numerical methods to be utilized are FEM for the magnetic field generation and CFD for the MHD interactions. The magnetic field will be obtained through Method 1 (described in §1.2). The CFD model will solve the MHD governing equations to capture the transient development of the flow field. The CFD software selection relied on the availability and the expansion of numerical models of the steelmaking processes at CIVS, which narrowed the selection to ANSYS FLUENT® for the fluid domain simulation. This chapter will present the governing equations for the physics involved and discuss the numerical methods.

2.1 Electromagnetic Theory

Electromagnetism has four primary founders: Gauss, Faraday, Ampére, and Maxwell. Maxwell was well-known for bringing the experimental work of Faraday into a more structured mathematical form, and correcting Ampére's law for electrodynamics. Maxwell's equations are the conglomeration of four laws that govern classical electromagnetism and are given in differential form for electrodynamics below:

$$\nabla \cdot \vec{E} = \frac{\rho_e}{\epsilon_o} \tag{2.1}$$

$$\nabla \cdot \vec{B} = 0 \tag{2.2}$$

$$\nabla \times \vec{E} = -\frac{\partial \vec{B}}{\partial t} \tag{2.3}$$

$$\nabla \times \vec{B} = \mu \vec{J} + \mu_o \epsilon_o \frac{\partial \vec{E}}{\partial t} \tag{2.4}$$

Gauss's law, Eq. (2.1) where $\vec{E}$ is the electric field, ρ_e is the total charge density (free and bound charges), and ϵ_o is called the permitivity of free space, describes

the connection between electric field flux and charge density. It follows that the flux through a closed surface is a measure of the total charge contained within that surface. It is easier to conceptualize through the integral form, but due to the nature of MHD, volumetric charge densities will be more helpful than line or surface charge distributions. Eq. (2.2) is a statement without a proper name, formed on the basis of the solenoidal characteristics of magnetic fields, where $\vec{B}$ denotes the magnetic field[1]. This statement arises from nonexistence of magnetic monopoles. Magnetic fields curl, meaning the divergence is zero for any magnetic field. Faraday's law of induction, Eq. (2.3), describes induced electric fields due to a changing magnetic field. This phenomena occurs in order to preserve a constant magnetic flux through a given surface. Ampére's original law is Eq. (2.4) without the last term, which is formulated for electrostatics, where μ_o is the permeability of free space and $\vec{J}$ is the current density vector. The last term was added by Maxwell to account for electrodynamic systems and to satisfy Eq. (2.14), and is called the displacement current. This law gives the relation between the magnetic field around a loop due to the amount of current passing through the surface enclosed by the loop.

The governing equations have been presented, but the fundamental concepts of electromagnetic theory are more easily grasped when discussing the effects of electromagnetic forces on charged particles. In particular, the electrostatic and magnetostatic forces. Not only does this benefit for providing insight but also for understanding the fundamental phenomena that MHD relies on. This discussion will start by covering electrostatics due to the simplicity.

2.1.1 Electrostatics

At the elemental level, charges are positive or negative, both of which emit electric fields, shown in Fig. (2.1). The interactions among these charged particles are gov-

---

[1]Many authors call $\vec{H}$ the "magnetic field" and rename $\vec{B}$ the "flux density" or some other term. This is confusion needs to be put to an end. Therefore, I will continue to denote the magnetic field as $\vec{B}$. $\vec{H}$ will be known as the auxiliary field; see David Griffith's excerpt on page 271 [12].

erned by the notion that opposite charges attract and like charges repel one another. In electrostatics, these charged particles are confined to a fixed position. An ensemble of similarly charged particles can produce a strong electric field due to the additive properties.

(a) Positive Charge   (b) Negative Charge
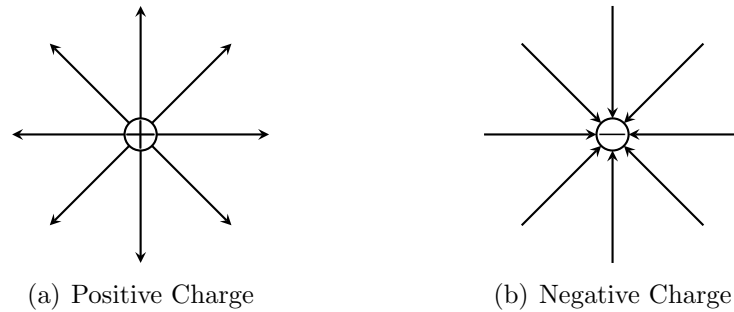
Fig. 2.1: Electric fields due to charged particles.

A common example of a charge ensemble is a parallel plate capacitor, see Fig. (2.2). The top plate holds negative charges while the bottom plate contains positive charges forming a voltage difference. Note that the fields above and below the plates will cancel with each other.
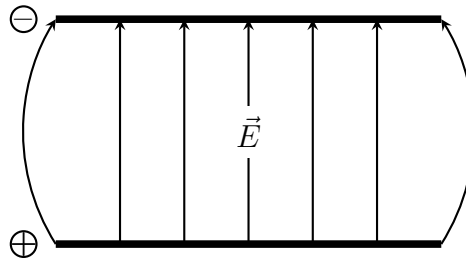
Fig. 2.2: Electric field of a parallel plate capacitor.

Fig. (2.2) shows the edge effects of the electric field between the plates. This results from the charge field lines at each end of the charged plates. Just imagine the field lines emitting as in Fig. (2.1a) at the bottom left corner; it would begin to diverge but the field line would be attached to the upper plate, bringing it back in. The important aspect here is that a uniform field is obtained within the capacitor,

away from the edge effect regions. These systems are normally utilized for charge storage but can also be used for particle path manipulation.

2.1.2 Electrodynamics of a Charged Particle

The most basic example of electrodynamics[2] comes into the picture once a charged particle begins to move. For example, if there was a positively charged particle traveling at a given velocity within an external electric field, the trajectory would be changed, shown in Fig. (2.3) (edge effects of the field are ignored for simplicity). This is caused by the force between the electric field and charged particle. This particle within a uniform field would be under the influence of the Coulomb force, $\vec{F}_C$, given by

$$\vec{F}_C = q\vec{E} \tag{2.5}$$

where $\vec{E}$ is the electric field vector and q is the charge value.
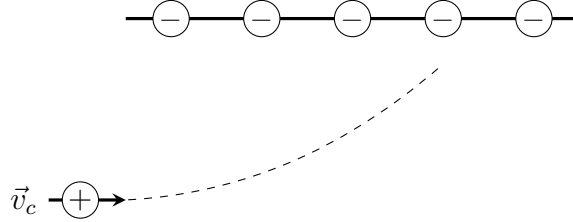
Fig. 2.3: Uniform external electric field interaction with charged particle.

A charged particle moving with a velocity $\vec{v}_c$ within a uniform magnetic field would experience a force of

$$\vec{F}_B = q(\vec{v}_c \times \vec{B}) \tag{2.6}$$

The more interesting aspect of these two interactions is when they are combined within one domain, see Fig. (2.4). This figure shows the magnetic field, $\vec{B}$, penetrating

---

[2]This is categorized within the realm of classical electrodynamics since the charged particle is in motion, where previous discussion focused on stationary charges.

into the page (indicated by $\otimes$), an electric field directed down the page, and the motion of a positively charged particle from left to right. There are now two forces acting upon the particle. This phenomena is governed by the Lorentz force given by

$$\vec{F}_L = q[\vec{E} + (\vec{v}_c \times \vec{B})] \tag{2.7}$$

For the case shown in Fig. (2.4), the particles path is strictly maintained horizontally. This is occurs when the magnetic and electric fields equally contribute in opposite directions. The particles trajectory can be precisely set by varying either the magnetic or electric field strength[3].
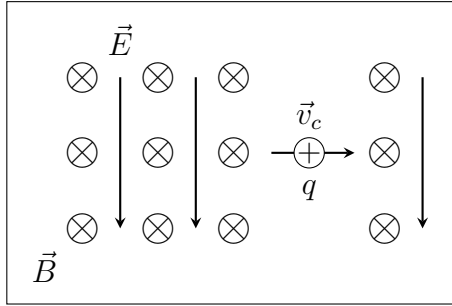
Fig. 2.4: Lorentz force diagram.

Now, true electrodynamics can be introduced into the system in Fig. (2.4) if there is a transient magnetic field present. This will introduce a secondary electric field giving the force on the particle the form of

$$\vec{F} = q[\vec{E} + \vec{E}_i + (\vec{v}_c \times \vec{B})] \tag{2.8}$$

where $\vec{E}_i$ is the induced electric field from the time-dependent magnetic field. Two takeaways are that the induced electric field is divergent free, $\nabla \cdot \vec{E}_i = 0$, which does not follow Eq. (2.1) since it is induced, see [9].

---

[3]This was first used for isotope separation during the Manhattan Project, and is the basis for how mass spectrometers work.

2.1.3   Wave Representation

Electric and magnetic fields can be described as waves. The general wave equation is given by

$$\frac{\partial^2 \Psi}{\partial t^2} = V^2 \nabla^2 \Psi \tag{2.9}$$

where Ψ is a scalar function and V is the velocity at which the wave is traveling. Ψ can represent the pressure in a liquid or the magnetic field as it travels. For a light wave $V = c$. Reducing this to one-dimension and solving provides the general wave propagation equation:

$$\Psi(x,t) = A\cos(\omega t - kx - \phi_s) \tag{2.10}$$

where A is the amplitude of the wave, ω is the angular frequency which relates to the frequency through $\omega = 2\pi f$, k is the wave number given by $k = 2\pi/\lambda$ (where λ is the wavelength), and ϕ_s is the phase shift.

Eq. (2.10) is a cosinusoidal function that varies with time. It is common practice to transform time-dependent sinusoidal and cosinusoidal functions into exponential functions to easily manipulate integrals and derivatives[4]. Transforming these functions to be time-independent exponential functions is called phasor notation which operates within the phasor domain. Once the calculus operations are complete, the solution may be transformed back into the time domain. For example, a EMS unit produces a TMF. This is an AC field which has real and imaginary components that can be described by the wave equation:

$$B_i(\vec{r},t) = B_{o,i}(\vec{r})\cos(\omega t - \phi_s) + jB_{o,i}(\vec{r})\sin(\omega t - \phi_s) \tag{2.11}$$

where i indices the coordinates x, y, z at a given time, the imaginary unit is represented by j, and $B_{o,i}$ is the amplitude of the wave. Eq. (2.11) in phasor notation becomes

---

[4]This form is also used for ease of data exportation and importation, see [13].

$$B_i(\vec{r}) = \mathrm{Re}\left\{B_{o,i}(\vec{r})e^{-j\phi_i(\vec{r})}\right\} + j\,\mathrm{Im}\left\{B_{o,i}(\vec{r})e^{-j\phi_i(\vec{r})}\right\} \tag{2.12}$$

Notice that the phasor form is only spatial and phase dependent.

2.1.4 Fields in Matter

Up until now, the only effects considered are the charge interactions with fields. In most practical applications, the charges will be carried within a medium with material properties that affect the strength of the fields interacting with the charges. In an Ohmic conductor (most conducting materials are considered Ohmic) the current density, $\vec{J}$, is given by Ohm's law:

$$\vec{J} = \sigma\vec{E} \tag{2.13}$$

where σ is the electrical conductivity. This leads to the conservation of charge given by

$$\nabla \cdot \vec{J} = -\frac{\partial \rho_e}{\partial t} \tag{2.14}$$

stating that the change of charge in a region is the result of the amount of charge passing through the surface of that region. This expression is directly derived from Maxwell's equations and it is not an independent assumption [12]. Charges can be destroyed and created but the overall quantity must be constant, unlike the conservation laws shown in §2.2. Note that this continuity statement is regarding local charge conservation.

The source of the current density is dependent on the material. If the material is magnetic, then $\vec{J}$ can have two sources[5] adding together yielding

$$\vec{J} = \vec{J_b} + \vec{J_f}, \tag{2.15}$$

---

[5]The polarization of the material can also add $\vec{J_p}$ but this is not in the scope of this project.

where $\vec{J}_b$ and $\vec{J}_f$ are the bound and free current densities, respectively. The bound current density is due to magnetization of the material. This only occurs if the material is magnetic. The free current density is the excess charge flowing through the system unbound by the magnetization. A non-magnetic conductor that contains a nonzero net charge will have a charge distribution residing near the surface of the conductor. This is due to the repulsive nature of like charges. The system with free currents will be further discussed in §2.3.1.

Wave Attenuation

There are two overseeing categories that an electromagnetic wave can travel through: lossless and lossy mediums. Lossless mediums do not affect the wave as it travels through, but lossy mediums attenuate the amplitude of the wave by a factor of $e^{-\alpha x}$, where α is the attenuation constant and x is the distance into the medium. This alters Eq. (2.10) to the form:

$$\Psi(x,t) = Ae^{-\alpha x}\cos(\omega t - kx - \phi_s). \tag{2.16}$$

Most materials are categorized as a lossy medium which is determined through

$$\frac{\epsilon''}{\epsilon'} = \frac{\sigma}{\omega\epsilon}, \tag{2.17}$$

where ϵ'' and ϵ' are the imaginary and real components of the permittivity [14]. Permittivity is expressed by the permittivity of free space, ϵ_o, and the relative permittivity of the material, ϵ_r, through the constitutive relation:

$$\epsilon = \epsilon_r\epsilon_o. \tag{2.18}$$

The attenuation constant for a good conductor[6] is given by

$$\alpha = \sqrt{\pi f \mu \sigma}, \tag{2.19}$$

---

[6]In practice, a good conductor is categorized by $\epsilon''/\epsilon' > 10^2$ [14].

where the permeability, μ, is related to the relative permeability, μ_r, through another constitutive relation:

$$\mu = \mu_r \mu_o. \tag{2.20}$$

The attenuation constant is important in determining the distance at which $\Psi(\delta_s)$ divided by $\Psi(x_o)$ is equal to e^{-1} [14], where x_o is the distance where $\Psi(x)$ divided by the amplitude is unity (i.e. at the surface of the conductor). This distance is known as the skin depth, which measures how well an electromagnetic wave can penetrate a conductive medium and is described by

$$\delta_s = \frac{1}{\alpha} \tag{2.21}$$

2.1.5   Electromagnetic Flux Conservation

As stated earlier, Maxwell's laws are easier understood in integral form. Gauss' law relates the total charge enclosed within a closed surface and the resulting electric field. This is simply read through the integral form:

$$\Phi_E = \oiint_S \vec{E} \cdot d\vec{S} = \frac{Q_{\text{encl}}}{\epsilon} \tag{2.22}$$

where Q_{encl} is the total charge contained within the surface. This is measuring the electric field flux, Φ_E, through the closed surface. Ampére's law is analogous to Gauss' law but for magnetic fields. Ampére's law transformed into integral form through Stokes' law yields

$$\oint_C \vec{B} \cdot d\vec{l} = \mu \iint_S \vec{J} \cdot d\vec{S} = \mu I_{\text{encl}} \tag{2.23}$$

which relates the total electric current enclosed, I_{encl}, within a surface to the total amount of magnetic field around the current source. A more interesting phenomena

occurs if the closed area changes or the field strength changes. This is governed by Faraday's law, in integral form it is given by

$$\mathcal{E} = \oint_C \vec{E} \cdot dl = -\frac{\mathrm{d}}{\mathrm{d}t} \iint_S \vec{B} \cdot d\vec{S} = -\frac{\partial \Phi_B}{\partial t} \qquad (2.24)$$

stating that an electromotive force (EMF)[7], denoted by $\mathcal{E}$, is produced in the opposing direction of the rate of change of the magnetic field flux, Φ_B.
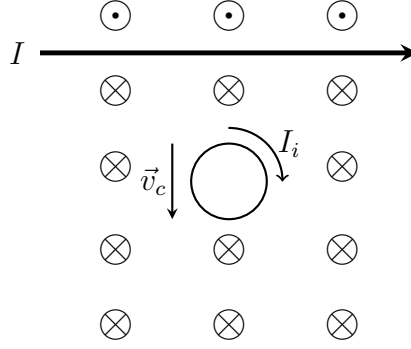
Fig. 2.5: Faraday's law for a falling loop.

This concept is better shown through Fig. (2.5). The loop is a conducting wire that encloses a constant area and is falling within a domain that contains a magnetic field. The magnetic field is created by the straight wire carrying the steady current I, which is governed by Ampére's law. As the loop falls further away, the magnetic field magnitude falls off by the inverse of the distance from the wire. This directly reduces the magnetic flux through the loop. The flux of the system must remain constant, therefore an induced current will be created within wire loop (driven by the EMF.). This induces an additional magnetic field around the wire directed into the page to maintain the original flux density through the area of the loop. This is the essence of Faraday's law, which plays a crucial role in the study of MHD.

---

[7]The 'force' term in S is not given in the sense of forces between bodies, rather it describes the driving force that is imparted as the result of flux conservation, see Fig. (2.5).

2.2 Governing Fluid Flow Equations

The study of fluid flow is governed by three conservation laws: conservation of mass, momentum, and energy. The relative governing equations are presented below, but the descriptions are concise to limit redundancy considering the copious amount of available references on this topic. The continuity equation in differential form is

$$\frac{\partial \rho}{\partial t} + \nabla \cdot (\rho \vec{V}) = 0 \tag{2.25}$$

where $\vec{V}$ is the velocity vector, and ρ is the density. The momentum equations, also called Navier-Stokes equations, for the x, y, and z directions are:

$$\frac{\partial(\rho u)}{\partial t} + \nabla \cdot (\rho u \vec{V}) = -\frac{\partial p}{\partial x} + \nabla \cdot (\mu \nabla u) + S_{Mx}$$
$$\frac{\partial(\rho v)}{\partial t} + \nabla \cdot (\rho v \vec{V}) = -\frac{\partial p}{\partial y} + \nabla \cdot (\mu \nabla v) + S_{My} \tag{2.26}$$
$$\frac{\partial(\rho w)}{\partial t} + \nabla \cdot (\rho w \vec{V}) = -\frac{\partial p}{\partial z} + \nabla \cdot (\mu \nabla w) + S_{Mz}$$

where u, v, and w are the respective velocities in the x, y, and z directions, p is the pressure term, μ is the viscosity, and S_{M_i} is a source term. The energy equation is not provided since this study is isothermal, therefore not applicable. Note that the governing equations were given in the conservative form due to the Eulerian method implementation in solving the flow, see §2.4.2.

A more useful expression of these governing equations is by putting them into a general form given by

$$\frac{\partial(\rho \phi)}{\partial t} + \nabla \cdot (\rho \phi \vec{V}) = \nabla \cdot (\Gamma \nabla \vec{V}) + S_\phi \tag{2.27}$$

where ϕ is the variable of interest (for the momentum equation it is one of the velocity components). Γ a material property such as the viscosity or thermal conductivity for the momentum or energy equation, respectively. This allows for a better understanding of how each term impacts ϕ within a finite fluid element. The first term governs the rate of increase within the element, the second looks at the net rate of flow out of

the element, the third term is the rate of increase due to diffusion, and the last term is the impact of the source terms. Applying Gauss' divergence theorem to Eq. (2.27) will produce the general integral form of

$$\frac{\partial}{\partial t}\iiint_V \rho\phi\, dV + \oiint_S \vec{n}\cdot(\rho\phi\vec{V})\, dS = \oiint_S \vec{n}\cdot(\Gamma\nabla\phi)\, dS + \iiint_V S_\phi\, dV \qquad (2.28)$$

This form is suited for the methods of CFD explained in §2.4.2. These conservation laws are based on the axiom that a quantity is conserved as it travels through a finite volume. Mass does not vanish and energy is transferred as it propagates throughout a system. These equations allows for determining how mass and energy is impacted and how it affects the domain.

2.3   Governing Equations of Magnetohydrodynamics

MHD governs the interactions between magnetic fields and fluids. The study of MHD concerns itself with fluids that are both non-magnetic and electrically conducting. The magnetic field may be shaped to obtain specific flow patterns as discussed in §1.1.3. The conductor, being that it is a fluid, introduces deviations from conventional electrodynamics. The constraints on the fluid type allows for simplifications on the governing equations of electrodynamics given in §2.1 to take affect.

2.3.1   Electrodynamics of Magnetohydrodynamics

The requirement of non-magnetic fluids dictates that there will be no bound charges within the system. Therefore, free currents will be responsible for the current density. Under these requirements, the charge density will be nonexistent in a stationary electrically conducting fluid. In MHD, the conductor will be moving which allows for a small amount of charge density to exist within. The charge density is too small to create a significant electrical force within the conductor [9], leaving the Lorentz

force responsible for the bulk motion. Therefore, the right-hand-side of Eq. (2.14) can be considered zero, changing the conservation law to

$$\nabla \cdot \vec{J} = 0 \tag{2.29}$$

The last term shown in Eq. (2.4) is negligible in the realm of MHD, therefore dropping it leads back to the original Ampére's law:

$$\nabla \times \vec{B} = \mu \vec{J} \tag{2.30}$$

This simplification is allowed since the displacement current term mainly exists to explain the propagation of a transient electric field. The only electric fields in MHD are the non-diverging induced fields from the time-dependent magnetic fields. For the concern of MHD, the charge density is very small, which renders Maxwell's correction to have minuscule affect on the system [9]. In addition, Gauss' law Eq. (2.1) is dropped from governing the impact on the flow due to ρ_e being small. This reduces the governing equations of electrodynamics for MHD to the follow three equations:

$$\nabla \times \vec{E} = -\frac{\partial \vec{B}}{\partial t} \tag{2.31}$$

$$\nabla \times \vec{B} = \mu \vec{J} \tag{2.32}$$

$$\vec{J} = \sigma(\vec{E} + \vec{V} \times \vec{B}) \tag{2.33}$$

these are Faraday's law, Ampére's law, and the current density for a moving fluid conductor, respectively. This is also constrained by solenoidal characteristic of magnetic fields.

The new form of the current density shown in Eq. (2.33) is obtained if the conductor is a fluid and is in a dynamic state within a domain that harbors external magnetic and electric fields. Current density is typically discussed for solid stationary conductors (e.g., circuit boards with Ohmic conductors) but it can be applied to the study of motional fluid conductors if set in a Lagrangian[8] frame of reference.

---

[8]See §2.4.2 for a further discussion on reference frames.

This is implemented by following the local velocity of a conducting fluid element and considering Newtonian relativity [9]. This means that the relative electric field, $\vec{E}_r$ measured in the frame of the fluid is equal to

$$\vec{E}_r = \vec{E} + (\vec{V} \times \vec{B}) \tag{2.34}$$

which is just the combination of two electric fields[9]. Multiplying the relative electric field by the conductivity gives the desired result of Eq. (2.33). Now that the previous equations have been presented, the volumetric Lorentz force, $\vec{F}_V$, can be defined by

$$\vec{F}_V = \vec{J} \times \vec{B} \tag{2.35}$$

which describes the Lorentz force in a fluid conductor moving within speeds pertaining to classical mechanics.

2.3.2 Magnetic Field Transport Equation

As shown earlier, the only three governing equations for electrodynamics in MHD are Ampére's law, Faraday's law, and the current density of a fluid. Combining these gives a relation for the advection and diffusion characteristics of $\vec{B}$ for MHD. The derivation shown in **Appendix A** concludes with

$$\frac{\partial \vec{B}}{\partial t} = \nabla \times (\vec{V} \times \vec{B}) + \lambda_B \nabla^2 \vec{B}, \quad \lambda_B = \frac{1}{\mu\sigma} \tag{2.36}$$

where λ_B is the magnetic diffusivity. The advection characteristics are described by the curl of the velocity and magnetic field cross product, and the diffusion of the system is governed by the Laplacian operator performed on the magnetic field. If the velocity is known then the spatial and temporal progression of the magnetic field is also known, [9].

A key point with MHD is that there are two magnetic fields within the system. There is the external magnetic field and the induced magnetic field denoted by $\vec{B}_o$

---

[9]This can be easily seen if the units are carried out for curl operation.

and $\vec{b}$, respectively. $\vec{B}_o$ is imposed on the system where $\vec{b}$ is induced as a result of the external magnetic field impacting the system. These two magnetic fields are additive which interact with the current density that drives the Lorentz force for bulk motion of the liquid conductor. The total magnetic field will be labeled as before given by

$$\vec{B} = \vec{B}_o + \vec{b} \tag{2.37}$$

Note that the forces altering the path shown in Fig. (2.4) were explicitly shown since they are the same principles that drive MHD. In this case, the charged particle would be replaced with a fluid conductor in motion within an external magnetic field. This creates a current density through Ampére's law within the conductor. Ultimately, this sets a cyclic process of the conductor being effected by two magnetic fields and the current density. The impact of the induced field will be discussed in the following sections.

2.3.3 Qualitative Description of Magnetohydrodynamics

Now that the governing equations have been presented for the electrodynamics of the system and the evolution of the magnetic field, a description of how these work in conjunction to alter a flow field will be provided. The MHD process has three major steps which couple the velocity and magnetic field:

1. The interaction between the external magnetic field and the motion of the conducting fluid create an EMF, Eq. (2.24).

2. Ampére's law, Eq. (2.32), states that there will be an induced magnetic field, $\vec{b}$, due to the induced current density $\vec{J}_i$.

3. The Lorentz force, Eq. (2.35), is generated through the interaction between $\vec{J}_i$ and the combined magnetic field, Eq. (2.37).

Step 2 describes that magnetic fields can be 'dragged' fluids and Step 3 states magnetic fields can pull on fluids [9]. The following section will focus on characteristic

relations that dictate the degree of the coupling between the velocity and magnetic field.

2.3.4 Characteristic Parameters

The first parameter is the characteristic length scale given by

$$l_c = \frac{V_{\text{Body}}}{A_{\text{Surf}}} \tag{2.38}$$

where V_{Body} and A_{Surf} are the volume and surface area of the conducting fluid. The characteristic length scale is a common parameter used to determine the expected behavior of the system. For MHD, l_c aids in determining the ratio of the external and induced magnetic field [9] through the relation:

$$\sigma V l_c \rightarrow \begin{cases} 0 & \vec{b} \text{ is negligible} \\ \infty & \vec{b} \text{ and } \vec{B_o} \text{ are on the same order} \end{cases}$$

This relation is dependent on three variables: conductivity, velocity, and characteristic length scale, which all put constraints on the result of the MHD interactions. If the conductivity or velocity of the fluid conductor is low, then the induced field will be small. l_c is used to correspond to a 'characteristic area'. The strength of a magnetic field produced is dependent upon the size of the area that contains the current density, Eq. (2.23). Therefore, if the length scale is small then the coupling between velocity and the induced magnetic field is weak compared to the external magnetic field. Note that the inverse of these conditions result in induced fields which highly impact the system. For liquid metals, the system tends to be closer to the first conditions and have high conductivity with smaller velocities and length scales. The relation provided above comes from the magnetic Reynolds number R_m, which is the magnitude of the ratio of the advection and diffusion terms in Eq. (2.36) yielding

$$R_m = \mu \sigma V l_c \tag{2.39}$$

Notice that R_m is the same as l_c with the addition of the permeability of the material. The magnetic Reynolds number is used in a similar manner to the fluid Reynolds number by distinguishing flow characteristics.

For liquid metal MHD [9], the velocity of a conductive fluid is constrained by the viscous forces that yield a velocity range of 0.01 [m/s] $\rightarrow$ 1 [m/s]. This results in a R_m range of 0.001 $\rightarrow$ 0.1 since liquid metals have a conductivity of the order $\sim 10^6$ [S/m] and a small l_c. This characterizes small scale (industry) liquid metal MHD has low magnetic Reynolds numbers. For low R_m values, the timescale is the damping time, τ, given by

$$\tau = \frac{\rho}{\sigma \|\vec{B}\|^2} \tag{2.40}$$

where $\|\vec{B}\|$ denotes the magnitude of the magnetic field vector. The damping is due to the energy of the system transferring the kinetic energy into Joule heating.

2.4 Numerical Methods

As mentioned earlier, this study will be carried out computationally. §2.2 introduced a set of nonlinear partial differential equations (PDEs) that describe the conservation of fluid flow. General analytic solutions for these equations have yet to be obtained. This is also true for a multitude of other complex physics phenomena. Analytic solutions may be obtained with simplifications such as neglecting viscosity (resulting in the Euler equation) along with reducing the dimensions of the problem to one to two dimensions while still capturing the physics involved. These methods have given proper insight in the past, however modern problems have risen in complexity and require higher accuracy. The simplifications previously utilized will not suffice for the majority of problems faced today.

A solution can be obtained through experimental testing or numerical solutions. Experimental testing requires probes, test rigs, and data analyses. Numerical approximations require high computational power, sophisticated and complex numer-

ical schemes, and data analyses. Experimental testing tends to be high cost and narrow-sighted, whereas numerical approximations can deliver a wide range of solutions. These numerical solutions are not limited to the geometry and conditions as in experimental testing. This can also provide foresight into new design variations, which is highly desirable for low cost changes during the developmental stages of a product. Now, these methods have been presented as three separate solutions to a problem when in actuality these methods should be used in conjunction to clarify the results of each. Theory is used for *verification* that experimental or numerical results match the physics involved. Experimental results should be used to *validate* the numerical results.

2.4.1   Electromagnetic Solver

The software selected for the electromagnetic simulation was ANSYS Electronics Desktop®. For details on mesh generation for this software see §3.2. This software offers plenty of project and solution types for simulating electromagnetic phenomena. The eddy current solver was selected (under the project type Maxwell 3D) to simulate the magnetic field. The eddy current solver uses a frequency domain to solve the generated magnetic field from the AC current sources. This solver is specialized for sinusoidal fields that are time-dependent, where the fields are created by AC currents with same frequency. This solver allows for individual phase shifts per current carrying conductor. The solution is solved within a computational domain referred to as a *region*. This region should be expanded out to infinity for an exact solution, however for simulation purposes the region is typically a set to be twenty percent larger than the simulated geometry.

The method in which the solution obtained is FEM. This is a numerical method for reducing ordinary differential equations (ODEs) or PDEs into algebraic expressions to be solved for an approximate solution to differential equation governing the phenomena. This allows a continuous function to be solved at discrete points within

the bounds of the system. The first step is to divide the computational domain into finite subdomains with node points and elements (e.g. a triangular element will have three node points, one at each vertex). This is known has discretizing the domain and the resultant discretized domain is called the mesh or grid. A solution to the discretized domain is accomplished by solving the algebraic expressions at each node. Once a solution is determined at each nodal point, a solution can be obtained at any point within an element formed by those nodes. FEM is a common method for structural analysis, heat transfer, and electromagnetics.

2.4.2   Computational Fluid Dynamics

The software selected for the fluid dynamic simulation was ANSYS FLUENT®. This software was used since ladle modeling at CIVS solely uses FLUENT®. CFD is commonly solved with three primary numerical methods: FEM, finite difference method (FDM), or finite volume method (FVM). FDM uses Taylor series expansions to approximate the differential equations. This method is the least accurate of the options. FEM can be used for fluid dynamics which some commercial softwares such as COMSOL Multiphysics®. FVM method uses finite control volumes called cells. This ensures that the flow into and out of the control volume is conserved. Most commercial softwares use FVM since the conservation of the flow through the finite volume is based on the same fundamentals as the conservation equations given in §2.2. Note that since the electromagnetic portion of this study will be completed with FEM, the electrodynamic governing equations are introduced in the differential form; where the fluid domain will be solved using the FVM method. This is why the general integral form of the conservation laws were presented at the end of §2.2.

Frame of Reference

The frame of reference selected for CFD is typically between the Eulerian or Lagrangian. The Lagrangian approach is accomplished by following the finite control

volume as it moves throughout the domain. This is best suited for particle tracing such as bubble injection. The Eulerian approach is common for fluid flows where the finite control volume is spatially fixed. The models used in this study are based in the Eulerian frame of reference.

Turbulence Modeling

When using CFD, there are several models to choose from to solve the physics involved. For instance, there are various turbulence models. For FLUENT®, the applicable turbulence models to describe the flow in this study are the k-ω shear-stress transport (SST) model, Large Eddy Simulation (LES) model, and k-ϵ model. The former two require higher computational cost over the k-ϵ model. The k-ω SST model was considered due to the incorporation of the near-wall region plus the far-field turbulence solved by the k-ϵ. This would solve the flow development of the flow nearest to the EMS unit. As depicted in literature, the EMS flow field is a vortex at the center of the steel phase that could be appropriately calculated with the LES model. The k-ϵ was chosen above the other models due to the lower computational cost, the focus on capturing large eddies far from the walls, and the fact that the k-ϵ model is the most commonly used turbulence model for computational studies on EMS, [10], [11], [3]. The k-ϵ model is described by two equations, one for the turbulent kinetic energy (k) given by

$$\frac{\partial}{\partial t} + \frac{\partial}{\partial x_i} = \frac{\partial}{\partial x_j}\left[\left(\mu + \frac{\mu_t}{\sigma_k}\right)\frac{\partial k}{\partial x_j}\right] + G_k + G_b - \rho\epsilon - Y_M + S_k \qquad (2.41)$$

and the turbulent kinetic energy dissipation rate (ϵ) is described by

$$\frac{\partial}{\partial t} + \frac{\partial}{\partial x_i} = \frac{\partial}{\partial x_j}\left[\left(\mu + \frac{\mu_t}{\sigma_\epsilon}\right)\frac{\partial \epsilon}{\partial x_j}\right] + C_{1,\epsilon}\frac{\epsilon}{k}(G_k + C_{3,\epsilon}G_b) + C_{2,\epsilon}\rho\frac{\epsilon^2}{k} + S_\epsilon \qquad (2.42)$$

where G_k and G_b are the generation of turbulent kinetic energy relate to the velocity gradients and buoyancy, respectively. Constants are denoted by C and sources by S. σ_k and σ_ϵ are the turbulent Prandtl numbers for k and ϵ, respectively.

Multiphase Modeling

The fluid domain concerns itself with three phases: air, slag, and steel. The time-dependent volume of fluid (VOF) method was used to model the surface interactions between the three phases. This model was used over the Eulerian or mixture multiphase models due to the compatibility with the MHD module. This model solves the continuity equation for each phase. Near an interface, the VOF method applies interpolation schemes to determine the volume fraction of a phase within a cell. The interfaces between each phase is tracked through the solution of the continuity equation for the volume fraction of the phases. The model also included the surface tension affects. Turbulence is shared by the phases throughout the domain through a single set of transport equations along with the turbulence variables.

MHD Solver

The MHD phenomena is solved through the FLUENT® MHD module which is an add-on module to the ANSYS FLUENT® software. The MHD equations can be solved through the Magnetic Induction Method or the Electric Potential Method. This study focused on the Magnetic Induction Method since the magnetic field was generated in ANSYS Electronics Desktop®. This method solves for the induced magnetic field, $\vec{b}$, in Eq. (2.36), the induced current density, and the resulting volumetric Lorentz force, which is used as a source term in the momentum equation.

The manual for the MHD Module has a note about a scaling factor for the external magnetic field. The manual claims that the scaling factor aids in reaching convergence. The scaling factor will gradually increase the MHD effect to its actual magnitude through a series of restarts. The only clue for implementation given by the module manual was: if the external magnetic field magnitude is strong, it is advised to start with a small scale factor [13]. This implies that a small field requires a large scaling factor. For a study on the physical constraints of the scaling factor see §4.2.5.

2.4.3 Computational Resources

It was not until the 1990's when computers contained enough memory and computational power to solve numerical solutions in three-dimensions [15]. For CFD simulations on this order of complexity, it is typical for clusters of computer processors to be used in parallel computing to solve the system within a reasonable time frame. The computational resources used for this study are given in Table (2.1).

The majority of the studies were completed with parallel processing where the computational domain was divided among the number of processors used. The isothermal three-dimensional MHD fluid flow simulation typically used 80 processors on high performance computing (HPC) RICE cluster at Purdue University. The wall time, which is nomenclature for computational run time, was near 96-120 hours to obtain $\sim$25 seconds of simulated time while using the HPC resource. The electromagnetic simulation was solved on the local machine resulting in a runtime under 20 minutes.

Table 2.1: Local & HPC machine specifications.

Item	Local	RICE Cluster
CPU	Intel Xeon @ 2.20 GHz	Intel Xeon-E5
Cores	20	20/Node
RAM [GB]	32	64/Node

3. GEOMETRY AND BOUNDARY CONDITIONS

The major components for the simplified ladle are shown in Fig. (3.1). The taper angle denoted by θ, is typically near 3-5 degrees for metallurgical ladles. The geometry was created in ANSYS Workbench and ANSYS Electronics Desktop®.
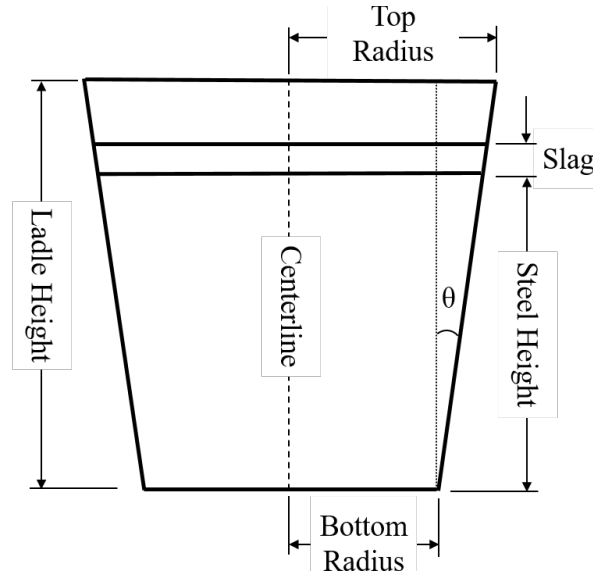
Fig. 3.1: General ladle dimensions.

This study is concerned with two simplified ladle designs given in Table (3.1). Case I is purposed for validating the model through comparison to literature results [10]. Case II uses a simplified ladle based on an industry drawings for further comparison.

Table 3.1: Ladle dimensions.

Ladle Dimension	Case I	Case II
Top Radius [m]	1.425	1.79
Bottom Radius [m]	1.425	1.62
Steel Height [m]	2.80	2.46
Slag Thickness [m]	0.1	0.15
Taper Angle [deg]	0	3
Tonnage [Tonne]	128.6	157.1

The positioning of the induction coil unit (LF-EMS unit) is set to the general location as depicted in Fig. (3.2a) and Fig. (3.2b). The dotted lines represent the ZY and XY planes which will be referenced from here onward. The dashed object in both figures is the LF-EMS unit. The vertical positioning of the LF-EMS set to encompass the steel phase region.

(a) Top view with reference planes. (b) ZY symmetry plane.
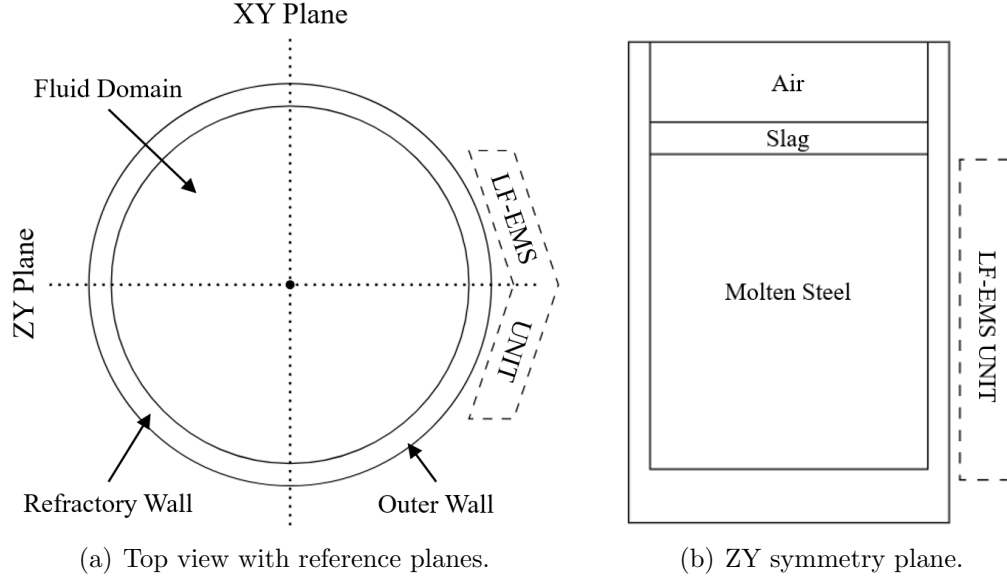
Fig. 3.2: LF-EMS unit position and reference planes.

3.1 Induction Coil Geometry

This section will cover the assembly of polyphase induction coil system that will generate the TMF. The height of the coil system was determined to be 246 [m] from an industry provided drawing. Some assumptions were made for the LF-EMS geometry such as the separation angle and span of the coil system, see Fig. (3.3).
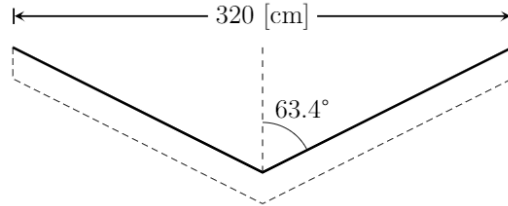
Fig. 3.3: LF-EMS unit span.

The coil system depicted in Fig. (3.4a) has important features pertaining to computational requirements versus reality. The region between the dashed black lines creates the bulk of the magnetic field in the fluid domain. The coils between the dashed lines are responsible for the prominent magnetic field generation. The extended portions are used for anodes and cathodes in the simulation. ANSYS Electronics Desktop® requires that the current source, for non-looping coils, be set to interface with the *region*, see §2.4.1. This allows the software to set an input and output current source at the ends of the coils, which act as the anodes and cathodes. The coils were set to the default material properties for copper.

(a) Extended coil system for simulation.

(b) Prominent coil region aside the fluid domain.
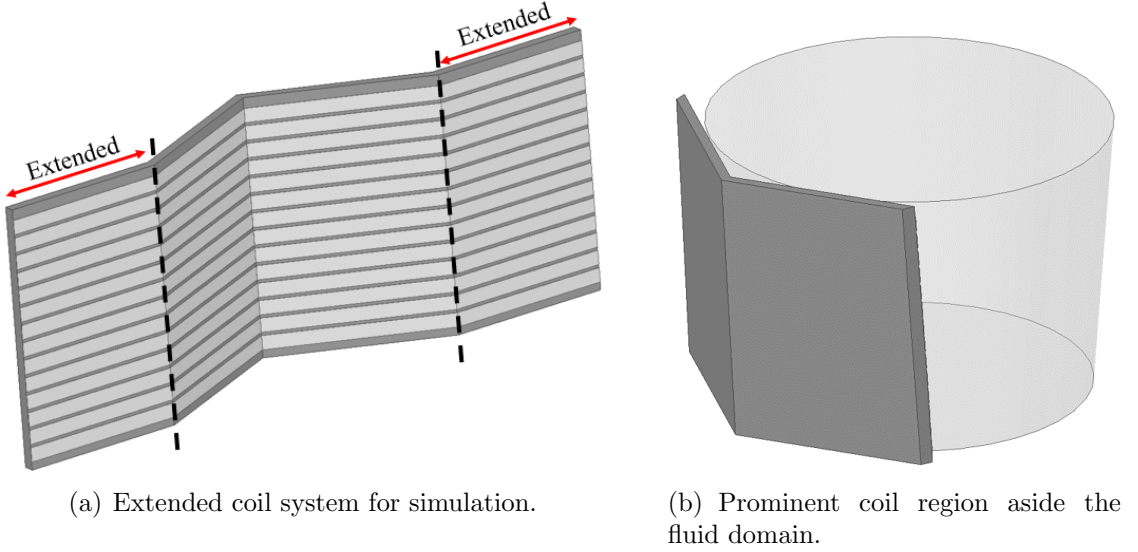
Fig. 3.4: LF-EMS unit.

The coils are colored in a light grey and the dark grey backing is included for aesthetics. In reality, the iron core is used to strengthen a DC magnetic field that magnetically saturates the ladle wall and allows the AC field to penetrate the wall without reducing the field strength. For simulation simplicity, the DC field and ladle wall are neglected. The dimensions and count of the current carrying coils were obtained through extracting values from industry drawings, see Table (3.2).
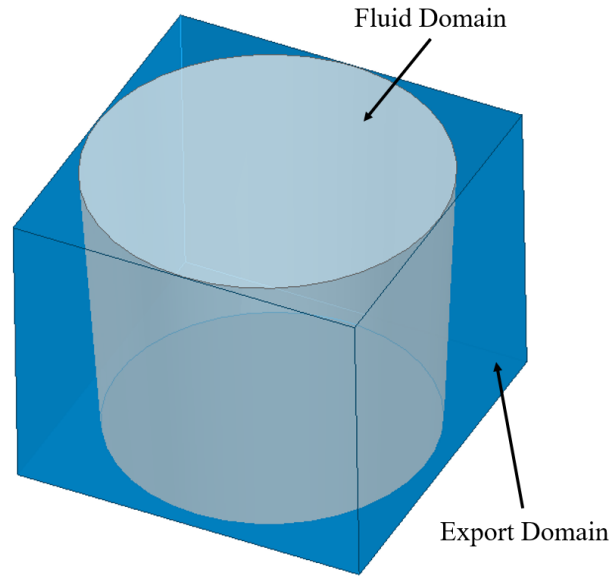
Fig. 3.5: Magnetic field export domain.

The simulated geometry has four major components: the solution region, ladle geometry (fluid domain), LF-EMS unit, and magnetic field export domain. The approximate solution for the magnetic field is solved within the solution region, see red outline in Fig. (3.6). The fluid domain only considers the steel phase since the magnetic field is invisible in all other phases. The LF-EMS unit generates the magnetic field and can be translated to fit various taper angles and radii. The export domain is used to separately extract the real and complex components of the magnetic field which will be used in the CFD simulation, see Fig. (3.5). The data are exported in Cartesian coordinates in phasor notation and then formatted with in-house code, see **Appendix B**. Once the data are in proper format, the magnetic field data file can be imported into FLUENT® through the MHD module, where it is automatically trimmed to only exist within the fluid domain.

3.2   Discretization of the Magnetic Field Domain

The mesh for the electromagnetic simulation and fluid domain are generated separately. ANSYS Electronics Desktop® has a user limiting meshing method that can be

altered by setting a maximum number of elements or an element size. This software automatically refines the mesh by solving the solution multiple times and comparing the error where the allotted error is guided by a set tolerance. For transient simulations, the mesher requires that one object has a mesh constraint defined. A maximum element length of 10 [cm] was used on the coils. The solution was solved two times for mesh refinement with a tolerance of 30%. The domain was discretized with tetrahedral elements and contained a final element count of 117,425 for the case II geometry. A mesh study was not required for the magnetic field simulation since the magnetic field cannot be compared one-to-one. The specifications in a production LF-EMS unit will not be disclosed by a manufacturer, therefore a mesh sensitivity study will not be a fruitful effort. Reduction of computational time for magnetic field generation is more important rather than the accuracy of the magnetic field data since the magnetic field is a general TMF generated for a numerical study.
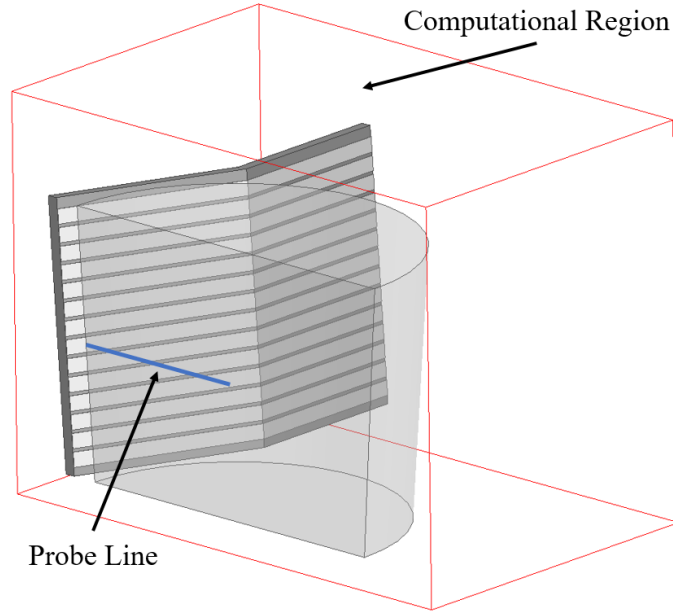
Fig. 3.6: Computational region symmetry clip with probe line.

An important parameter for electromagnetic fields traveling within a conductive medium is the skin depth, Eq. (2.21). As mentioned previously, the skin depth measures how far a electromagnetic field can penetrate before it falls off by e^{-1}. This

parameter in this study serves two purposes: verification that the mesh used in the electromagnetic simulation is suitable, and mesh refinement in the CFD simulation to capture the effective stirring region, see §3.5. The skin depth is obtained from the simulation by taking a horizontal probe line of the magnetic field magnitude from the wall surface into the steel phase shown in Fig. (3.6). Note that the magnetic field can be generated in either a conductive or non-conductive medium. The FLUENT® MHD module has different methods for working with either case. The magnetic field was generated in a conductive medium to determine the skin depth; however, the magnetic fields for the CFD simulations were generated in a vacuum space (non-conductive). For the conductive simulation, the molten steel properties used are listed in Table (3.6).

3.3 Induction Coil Boundary Conditions

The electric current within the coil system determined the boundary conditions for the magnetic field simulation. The electrical current was required to be AC to form a specific magnetic field type for EMS. The magnetic field was selected to be a TMF for the straight stirring unit. For the baseline case, the electric current amplitude value was selected to be 1500 [A] which was near the 1350 [A] value found in the literature, [10]. The number of windings in ANSYS Electronics Desktop® sets the number of conductors in a single coil in the simulation. The number of windings was determined by selecting a current amperage of 1500 [A] and increasing the number of windings, starting from 1, until the magnetic field matched the magnitude range provided by an industry collaborator. The coils were selected to be a stranded (a coil type in ANSYS Electronics Desktop®) current carrying wire, which inhibits electrical eddy currents from forming. The electrical current phase shift, ϕ_s, between the coils was determined through use of a relation between a half-wavelength of sinusoidal wave and the number of coils. The phase shift per coil relates to the number of coils through the expression below:

$$\phi_s = \frac{180°}{\text{Number of Coils}} \tag{3.1}$$

This phase shift relation for the formation of TMF was found in literature [8]. The number of coils was extracted from a depiction of the coil system provided by an industry partner. This ensures that all of the coils produce a superpositioned magnetic field of a half-wavelength across the coil system, see Fig. (4.3d). The electric current [16] per winding is given by

$$I = I_o \cos(2\pi ft + \phi_s) \tag{3.2}$$

where I_o is the current amplitude and f is the operating frequency. The phase shift and cosinusoidal current provided above formulate the basis for generating a traveling magnetic field. An industry partner provided the optimal stirring frequency range.

Table 3.2: LF-EMS unit parameters.

Component	Specification
Field Type	TMF (AC)
Electric Current Amplitude	1050-1500 [A]
Windings per Coil	50
Phase Shift per Coil	12.857

3.4 Fluid Domain Geometry

The fluid domain is only concerned with the fluids and magnetic fields within the ladle. The ladle refractory and outer wall, Fig. (3.2a), of the ladle was not modeled, rather the inner radii were used to define the fluid domain within wall boundaries. This region contains the three phases: air, slag, and steel. The geometry will follow closely to the dimensions in Table (3.1), unless specified for a parametric study. Since the majority of EMS simulations in the literature reduce the geometry to a cylinder, this study aims to capture the impact of taper angle and tonnage on the resulting flow field. The orientation of the origins for both simulations must align for proper

implementation of the magnetic field data. The LF-EMS unit is set on the positive z-axis and the fluid domain is centered at the origin in both simulations.

3.5   Computational Fluid Dynamics Grid

Three different grid systems, based on hexahedral cell types, were used for the fluid domain. The first mesh, M1, was an unstructured mesh for initial testing of the CFD simulation, see Fig. (3.7a). This included small inflation layers to capture wall effect. More sophisticated mesh techniques were implemented to improve the mesh quality, orthogonality, and overall structure. This was accomplished by inserting a rectangular prism in the center of the cylinder and slicing the domain along the diagonals created by the opposite vertices of the rectangular prism. This resulted in a grid system that is sliced into five sections of four sided objects[1]. This restructuring is apparent in M2 and M3 for Fig. (3.8b) and Fig. (3.9b), which is a combination of an O-grid and a H-grid, forming a H-O grid.

(a) Isometric View.   (b) Top view.
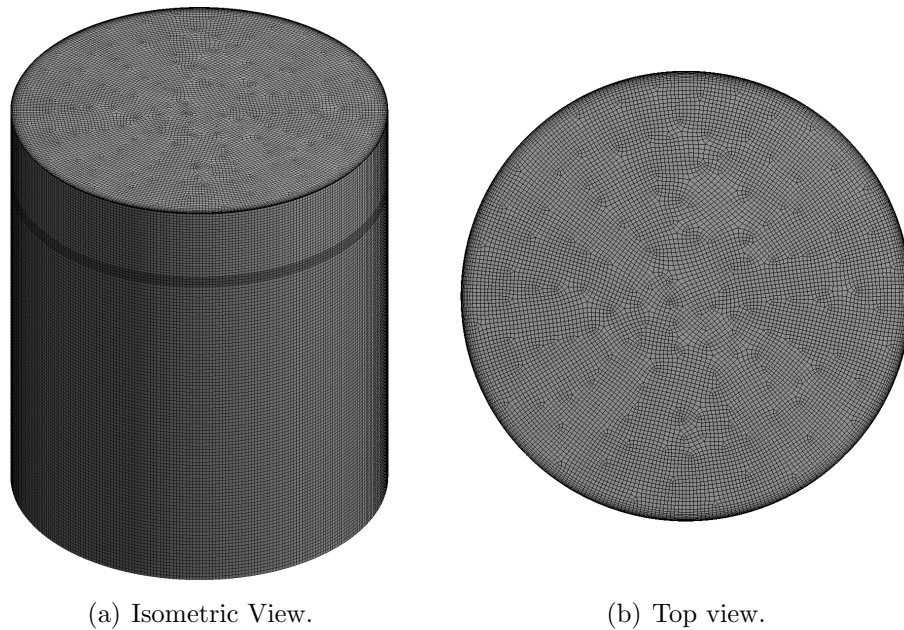
Fig. 3.7: Mesh: M1.

---

[1]Since structured cells are cuboids the domains that are discretized should also be close to cuboid shapes to maintain cell quality and orthogonality.

Mesh M2 did not include the inflation layers to test the importance of capturing the wall effect and skin depth. The inflation layers for M3 were based on total thickness which was set to the calculated skin depth through Eq. (2.21). These inflation layers were set to capture the effective stirring region that is restricted by the skin depth, since after this distance the magnetic field drastically drops off. The percent difference between M1 and M3 is less than than that of M2 and M3 at the developed flow due to M2 not including the inflation layers, shown in Table (3.3).

Table 3.3: Bulk velocity comparison per mesh at sample times.

Mesh	15 [s]	20 [s]	25 [s]	% Diff. from M3
M1	0.69	0.74	0.77	2.5
M2	0.71	0.80	0.82	3.8
M3	0.69	0.78	0.79	–
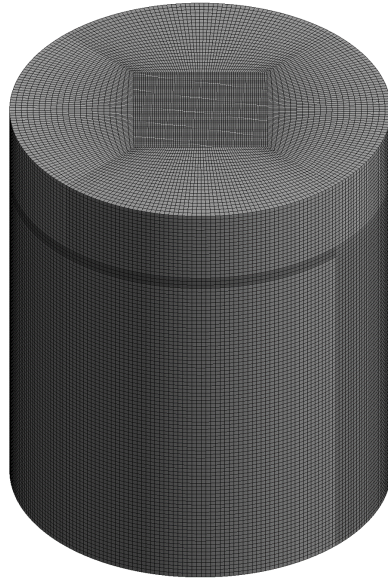
(a) Isometric View.   (b) Top view.

Fig. 3.8: Mesh: M2.

<div align="center">

(a) Isometric View.   (b) Top view.
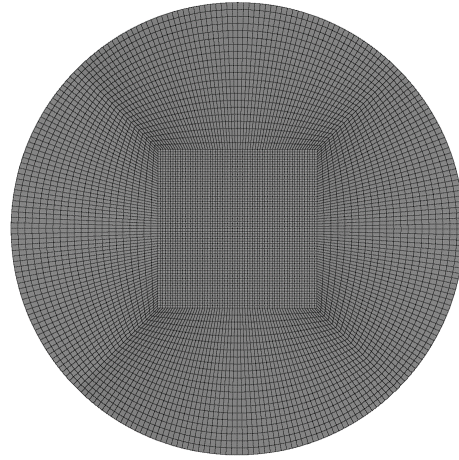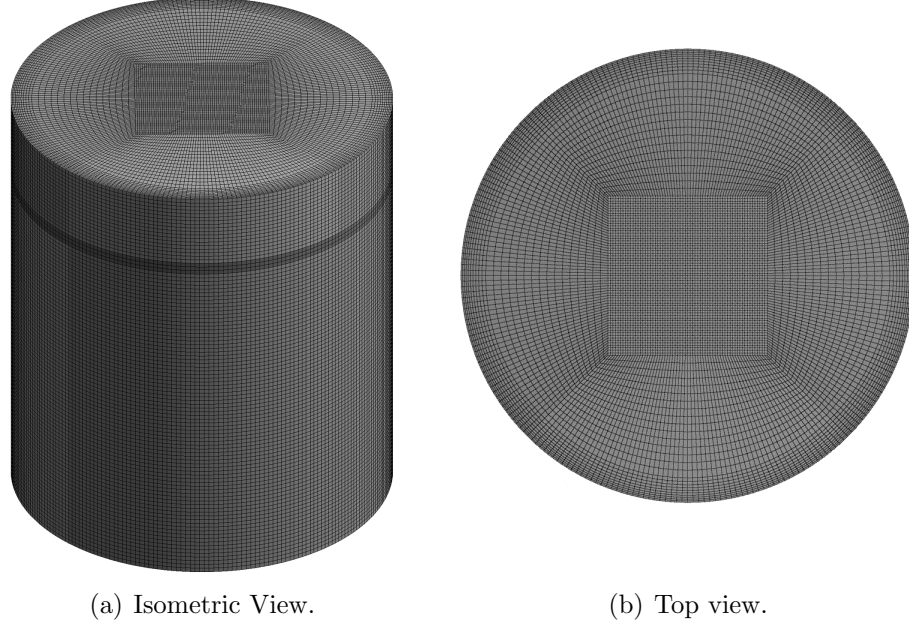
Fig. 3.9: Mesh: M3.

</div>

The inflation layers in M1 contained a first layer thickness of 2 [mm] with a growth rate of 1.27. The inflation layers were based on a maximum thickness of 0.155 [m] with a growth rate of 1.1 for M3. Both M1 and M3 had 10 inflation layers. As listed in Table (3.4), the structured grids reduced the element count by an average factor of 1.6 compared to M1. The inflation layers increased the cell count as expected, but the restructuring in M3 resulted in a factor of 1.13 more cells then in M2. The structured grids increased the minimum quality by nearly a factor of four, which resolved poor cell regions. The skewness and orthogonality did not vary significantly among the three grids.

<div align="center">

Table 3.4: Discretization parameters ($\Delta x = 3.5$ [cm]).

Component	M1	M2	M3
Number of Elements	1.61E6	9.57E5	1.09E6
Number of Nodes	1.65E6	9.79E5	1.11E6
Min. Quality	0.128	0.553	0.479

</div>

3.5.1   Timestep Considerations

Now that the spatial domain is discretized, the temporal portion of the simulation must be considered. The limiting factor of the timestep is either the velocity of the steel phase or the period of the TMF wave. To capture high velocity regions, if the projected maximum velocity is 2 [m/s] with a default cell length of 3.5 [cm] then the time for a fluid element to pass the cell length would be 0.0175 [s]. The magnetic field has a frequency of 1.5 [Hz]; therefore, the period is 0.667 [s]. To fully capture the magnetic field wave in a transient state, the timesteps should be at least a tenth of the period, resulting in a timestep of 0.06 [s]. The timestep was chosen to be 0.01 [s] to capture both the velocity of the system and the magnetic field wave while maintaining a reasonable computational cost. To verify this timestep is suitable, a calculation[2] of the Courant number, Eq. (3.3), resulted in a value of $C = 0.2$, where Δx is the typical length of a computational grid element.

$$C = \frac{V \Delta t}{\Delta x} \tag{3.3}$$

3.6   Boundary Conditions for Fluid Flow and Magnetohydrodynamics

A pressure-outlet condition is applied to the top of the ladle where the argon backflow is uninhibited. An operating density was enabled in order to aid in calculating the buoyancy forces in FLUENT®. This operating density was set to the lightest phase density (argon). The VOF phase hierarchy is shown in Table (3.5). The curved surface of the ladle and bottom are set as boundary walls. This model will be used in the future for combined EMGAS stirring; therefore, the air phase was set to properties of argon. The phases were introduced in the simulation by patching the volume fractions into the corresponding phase sections in FLUENT®.

---

[2]This calculation was concerned with the expected velocity for bulk motion of 0.7 [m/s], where $\Delta x = 3.5$ [cm] and $\Delta t = 0.01[s]$.

Table 3.5: Volume of Fluid phases.

Phase	Material
Primary	Molten Steel
Secondary I	Slag
Secondary II	Argon

The FLUENT® MHD module boundary conditions set the outlet and walls are insulating walls. This set the normal current density to be zero at the interface [13]. The material properties were set per phase, where the steel phase is the only electrically conducting medium. The relative magnetic permeability for all phases was set to unity.

Table 3.6: Material properties.

Property	Argon	Slag	Molten Steel
Density [kg/m^3]	1.225	2786	7200
Viscosity [kg/ms]	1.789E-5	9.4E-2	6.5E-3
Electrical Conductivity [S/m]	1E6	1E6	6.99E7

4. RESULTS

4.1 Magnetic Field Generation

Once the simulated magnetic field matched the provided magnitude range verification of the field was carried out through comparison between the theoretical and simulated skin depth. The fluid domain was set to the molten steel properties for this comparison. After the verification was complete, the fluid domain was set to vacuum space. The non-conductive medium was selected for the field generation to allow for different steel properties in the CFD simulation.
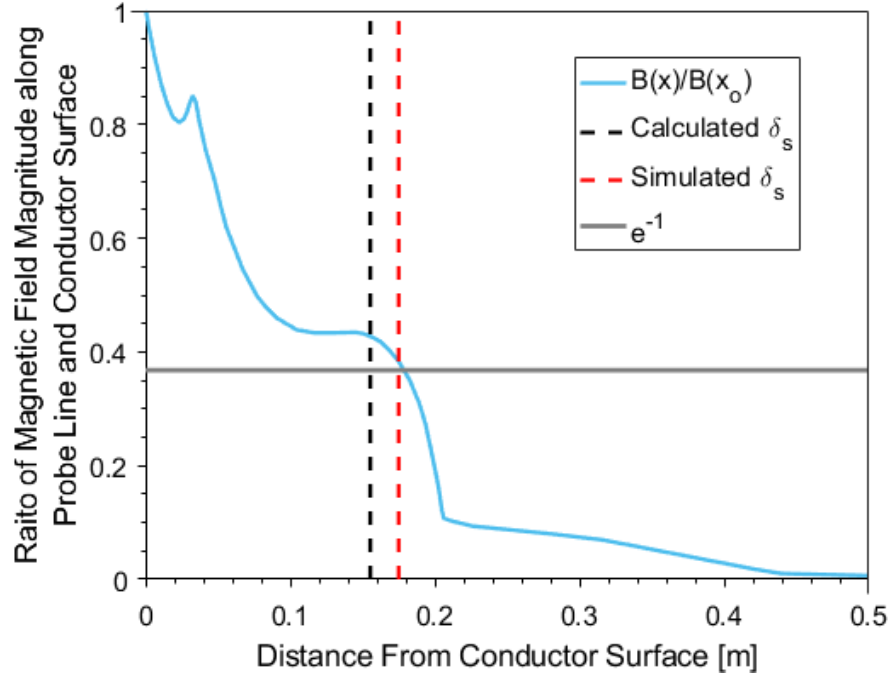
Fig. 4.1: Skin depth evaluation.

The skin depth for the steel phase is calculated to be $\delta_s = 0.155$ [m] with Eq. (2.21). Fig. (4.1) compares the ratio of the magnetic field magnitude along the probe line

to the magnetic field magnitude at the wall surface. This results in an 12.8% error between the theoretical and simulated skin depth. This verifies that grid captured the physics since the absolute difference of the skin depth was a mere 1.9 [cm].

4.1.1   Magnetic Field Distribution

The contours of the magnetic field are shown in Fig. (4.2a) through Fig. (4.2d) to obtain a sense of distribution on the nearest wall to the LF-EMS unit. The x-component of the field alternates between positive and negative values symmetrically on either side of the YZ-plane. The y-component is initially split with positive values existing in the top half of the steel domain and negative values for the lower half. The z-component is vertically symmetric. Fig. (4.2d) displays the combined magnetic field components on the wall surface.

(a) X-component.

(b) Y-component.

(c) Z-component.

(d) Magnitude.
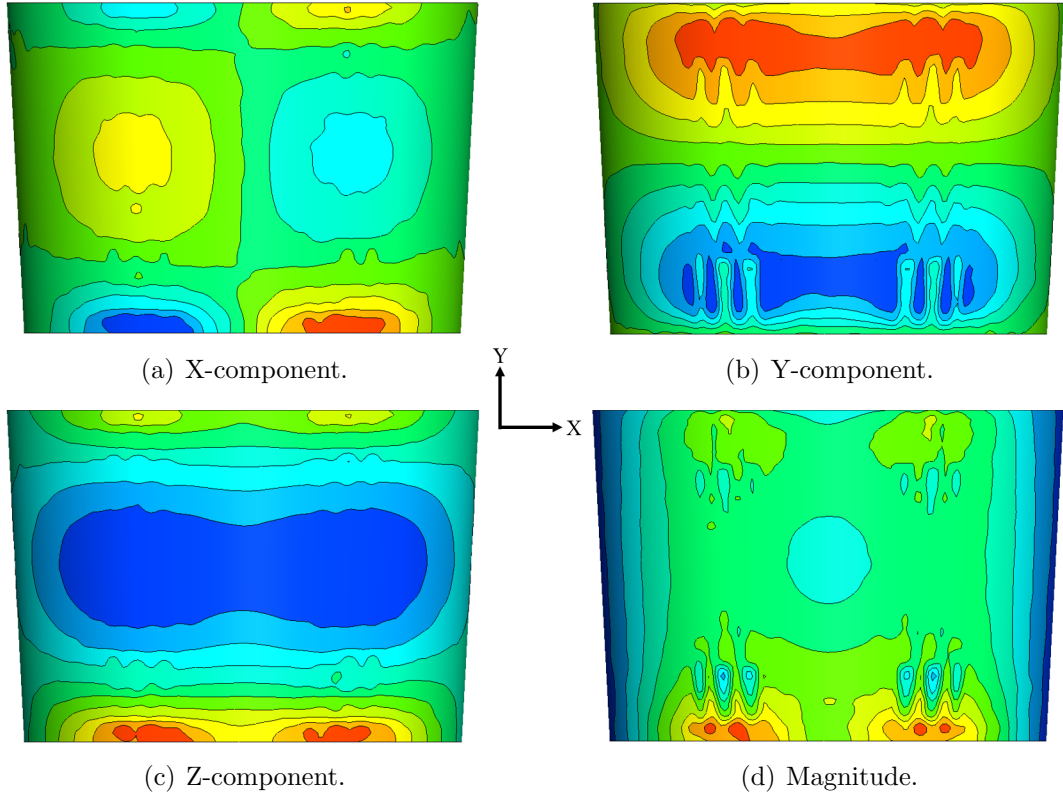
Fig. 4.2: External magnetic field contours on steel surface closest to LF-EMS unit ($I_o = 1500$ [A] at $t = 0$ [s]).

The magnetic field contours were plotted on the zy-plane to capture the transient behavior of the field. This plane splits the LF-EMS unit vertically in half. Fig. (4.3a) through Fig. (4.3f) displays the propagation of the wave as the phase increases. As mentioned earlier, the phases were selected from 0° to 180° to form a half-wave across the LF-EMS unit, this is shown best in Fig. (4.3d).

(a) Phase: 0°.   (b) Phase: 30°.   (c) Phase: 60°.

(d) Phase: 90°.   (e) Phase: 120°.   (f) Phase: 150°.
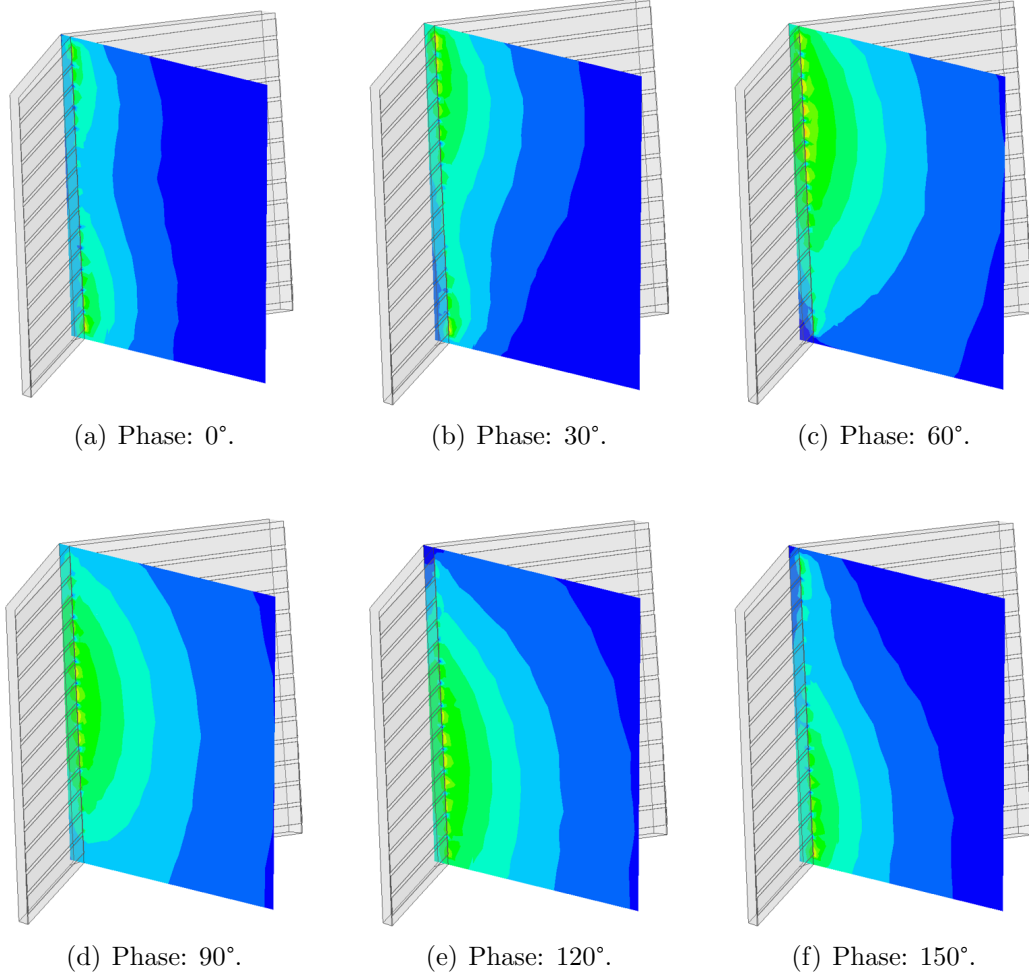
Fig. 4.3: Contour plots of TMF throughout phase shifts.

4.2   Multiphase Fluid Flow

The first consideration for the fluid flow was the strength of the coupling between the induced magnetic field and the velocity. The average characteristic length scale

for case I and II was ~ 0.5 [m]. The MHD of this system was characterized to be slightly over the low R_m range since the calculated value of R_m was 3.07. This means that the induced field and velocity will be a coupled system but not as strong as in astrophysics applications (i.e. dynamo theory). Note that the amperage range used produces a stirring force that creates slag-eyes. This departs from industrial EMS operating conditions where slag-eye formation is nonexistent. This was executed to encapsulate the stirring condition presented in literature, [10].

4.2.1 Mesh Study

The steel phase velocity development for three fluid domain meshes are compared in Fig. (4.4). Mesh M2 and M3 capture a similar curvature but M2 has a higher result. M1 is lower and falls away from the common trend with an additional convex drop. At 20s, M2 and M3 have a 1% difference and M1 varies from M3 by 2%. M3 was selected for future studies due to the mesh refinement criteria.
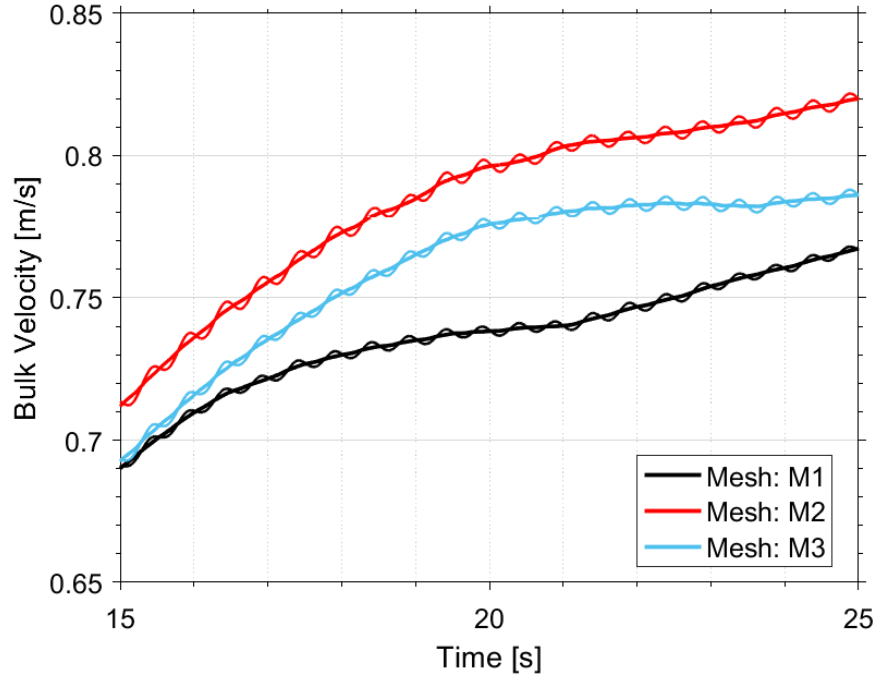
Fig. 4.4: Mesh study of bulk velocity. This figure also displays the raw data (oscillations) along with the post-processed data (smooth profiles).

Fig. (4.4) displays two lines per item to explain the numerical post-processing method used. Notice that the horizontal range in this figure has been trimmed to exemplify the oscillations throughout the velocity development. The ANSYS FLUENT® MHD module calculates an oscillating Lorentz force that is numerically unstable throughout the simulation [11]. These oscillations are the response to slight numerical over and under predictions of the Lorentz force generation. These oscillations have a maximum amplitude of 0.003 [m/s], which is 0.4% of the developed velocity magnitude. This is minuscule in comparison to the overall velocity formation. These oscillations were processed through a quarter-wavelength averaging scheme to produce the smooth curves shown in Fig. (4.4), see **Appendix C** for post-processing details. Note that the volume-averaged (bulk) velocity results shown from here onward will be processed through quarter-wavelength averaging.

4.2.2 Validation

Validation was obtained by comparing the bulk velocity of the steel phase and slag eye formation to another study completed by Sand et al. 2009 [10]. This study used the geometry from case I. This literature study contained a top slag layer to observed the impact on the slag eye formation. This method of implementing the MHD interactions was carried out through use of force density data paired with a semi-empirical formula to describe the evolution of the forces in the stirring direction. The literature presented that the bulk velocity for the steel phase was 0.7 [m/s] for downward stirring at an equilibrium time of 25 seconds. The results for this study was validated with experimental bubble modeling. The pumps were positioned to simulate the stirring patterns produced by EMS.

Table 4.1: Velocity development comparison with Sand et al. results at 1350 [A].

Study	10 [s]	15 [s]	20 [s]	25 [s]
Sand et al. [10]	0.530	0.634	0.663	0.713
Current Work	0.496	0.602	0.668	0.720

The comparison of the velocity development from the melt at rest to reaching quasi-equilibrium is given Fig. (4.5). The results are expected to inhibit variations since the solution was obtained by different methods. The variation in the bulk velocity development was primarily from 3 to 20 seconds with a maximum absolute difference of 0.08 [m/s]. Both methods resulted in a developed velocity within 25 seconds of stirring, at which the percent difference between the current work and Sand et al. [10] was 0.98% with an absolute difference of 0.007 [m/s]. The results were compared in a parity plot, Fig. (4.6), for a better representation of the differences.
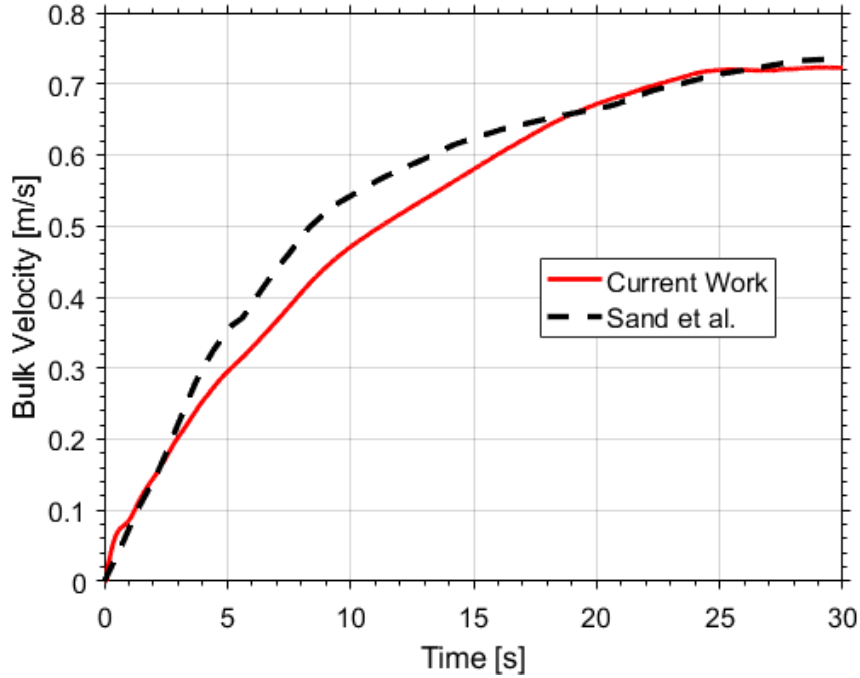
Fig. 4.5: Development of bulk velocity compared with literature, [10].

Another form of validation was determined through the multiphase behavior that was evaluated by the slag-eye development. The slag-eyes in Fig. (4.7a) and Fig. (4.7b) are the light grey sections. The literature presented that the cross-sectional area of the slag-eye was 1.55 [m^2] at 25 seconds and nearly 1.475 [m^2] at 35 seconds for the downward stirring results [10]. The flow is fully developed after 25 seconds; therefore, the area only changed slightly as time progressed (± 0.15 [m^2]). Note that

the results from this literature study for the area changes from 35s to 40s was not shown; however, the slag area was presented in Fig. (4.7b). Comparing the results at 25 seconds gives a difference of 25% with a absolute difference of 0.39 [m^2].
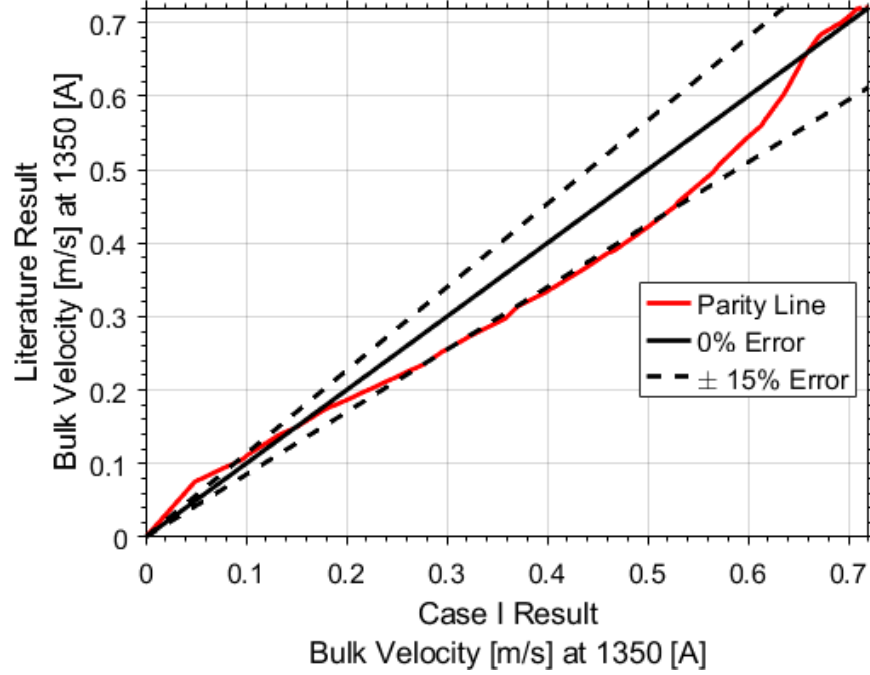
Fig. 4.6: Parity plot of bulk velocity.

Note that the slag-eye areas are slightly different in form but maintain similar features. This is due to the difference in magnetic field generation. Both fields are TMF; however, the electric current phases are most likely not a one-to-one match. More importantly, the literature result uses a semi-empirical force to update the transient force term. This method is most likely not capturing the dual circulation zones obtained from the vortex development. The sizes are relatively similar due to the same bulk velocity magnitude; however, this leads to a different flow field; therefore, a different slag-eye opening shape.

(a) Results at 25s.   (b) Sand et al. results at 40s [10].
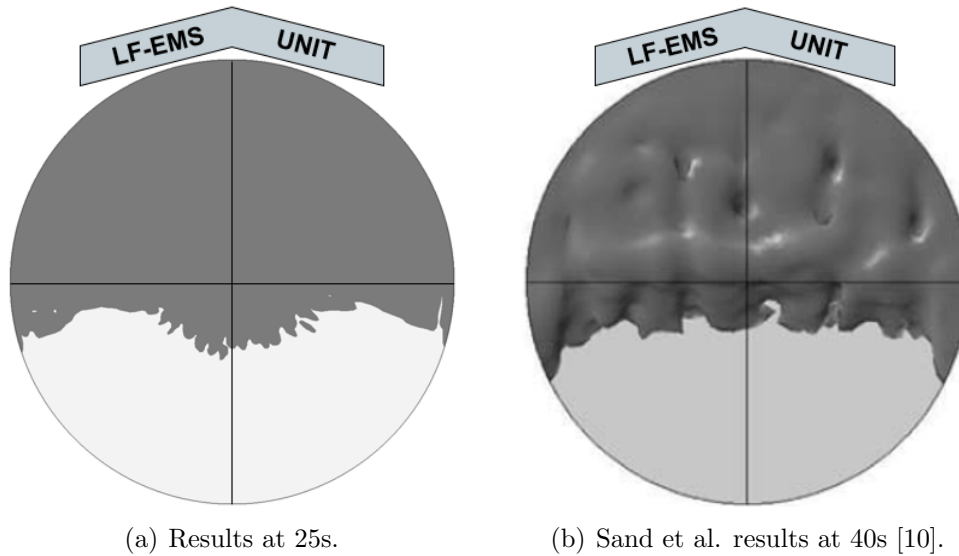
Fig. 4.7: Slag-eye comparison for downward stirring ($I_o = 1350$ [A]).

4.2.3 Vortex Formation

To obtain a better understanding of the flow development streamlines were used to represent the vortex formation in the steel phase. An amperage of 1500 [A] was selected for this observation. The vortex is symmetric about the zy-plane; therefore, only half of the streamlines are displayed for ease of visibility. The vortex development begins at the wall, nearest to the LF-EMS unit. This vortex has two primary components: the vortex core and the vortex arm. The center of the core remains fixed within the zy-plane and the vortex arm extends symmetrically from the zy-plane to the side walls. The vortex core travels from the front of the ladle to the back within the first 10 seconds as shown in Fig. (4.8a) and Fig. (4.8b). The first second of stirring produced a weak, tight vortex core and arm shown by the oval circulation and strands extending from the core to the left wall, respectively. At the 10 second mark, the vortex core and arms began to open up. From 15 to 20 seconds, the vortex core location settled in the center of the zy-plane, and the vortex arm expanded into a large circulation zone, as seen in Fig. (4.9a) and Fig. (4.9b). The circulation zone at the developed stage, 25 seconds, was more evenly distributed within the steel phase,

as seen in Fig. (4.10a). The core is comprised of two symmetric recirculation plumes on either side of the zy-plane, see Fig. (4.10b).

(a) 1 second.   (b) 10 Seconds.
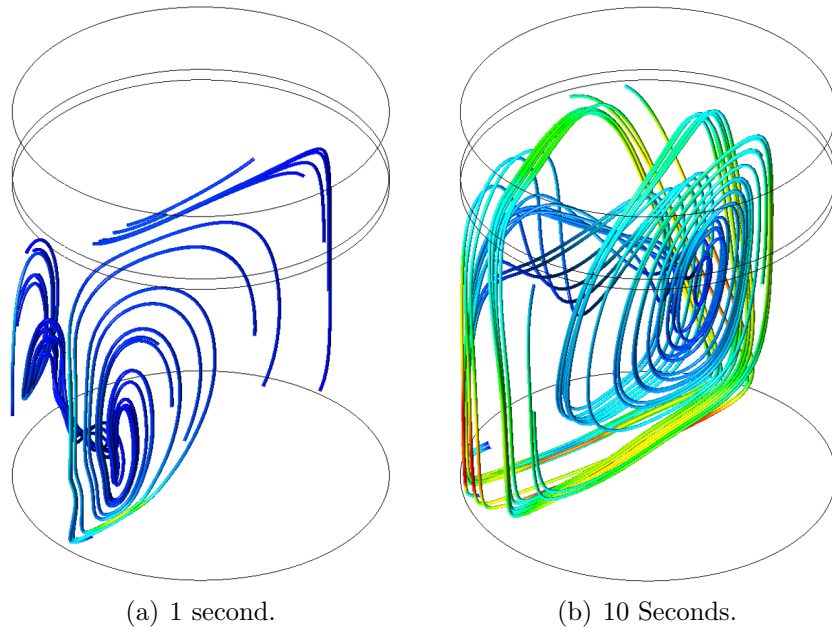
Fig. 4.8: Initial vortex formation.

(a) 15 seconds.   (b) 20 seconds.
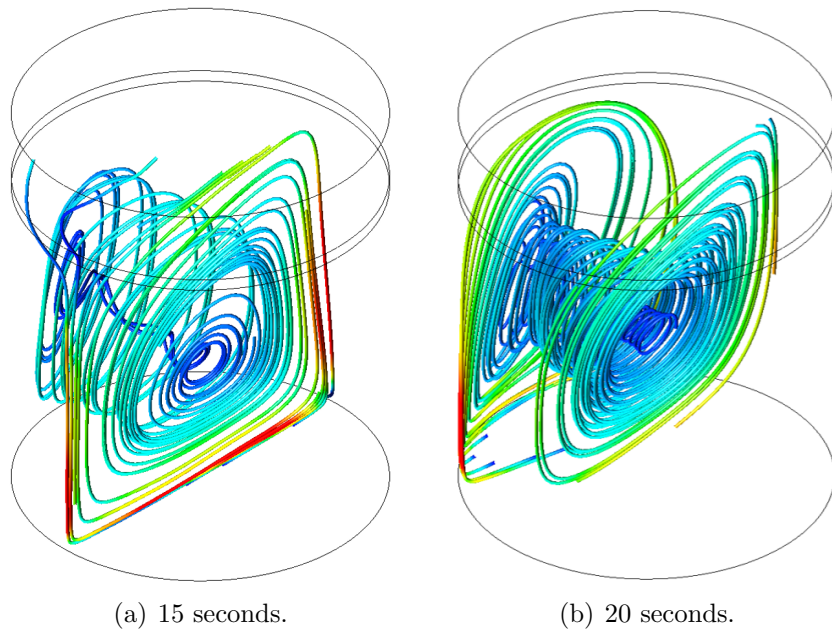
Fig. 4.9: Vortex growth and position settling.

(a) 25 seconds.   (b) Vortex core at 25 seconds.
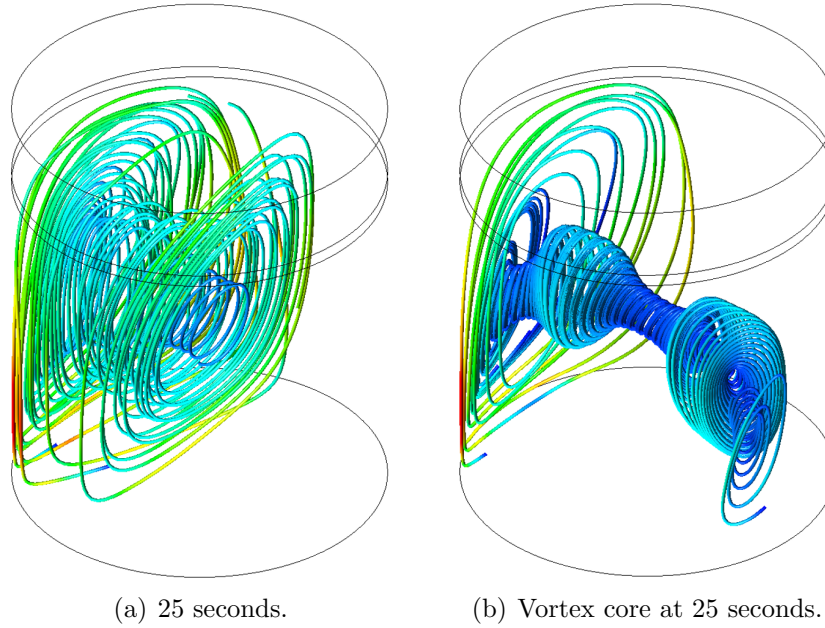
Fig. 4.10: Developed vortex.

4.2.4   Effect of Electric Current Amplitude on the Bulk Velocity

The previous section displayed the evolution of the vortex for an amperage of 1500 [A]. This vortex drives the bulk flow which depends on the strength of the magnetic field. The magnetic field magnitude is governed by the current amperage in the induction coils. Therefore, the results of a study on developed bulk velocity per variable amperage is given in Table (4.2). As expected, the bulk velocity decreases with decreasing amperage.

Table 4.2: Amperage impact on developed bulk velocity.

Amperage [A]	Velocity [m/s]
1500	0.786
1350	0.719
1200	0.609
1050	0.583

4.2.5   ANSYS FLUENT MHD Module Scaling Factor

The FLUENT$^®$ MHD manual states that the MHD scaling factor gradually increases the MHD effect to its actual magnitude through a series of restarts by scaling the external magnetic field, §2.4.2. The manual for the MHD Module has a sparse section about implementing a scaling factor for the external magnetic field. For this project, the scaling factor can be used to calibrate the MHD effects with the generated magnetic field since the flow time and developed velocity are known. This study sought to find the limitations of this scaling factor. The scaling factor will be denoted by S_f.
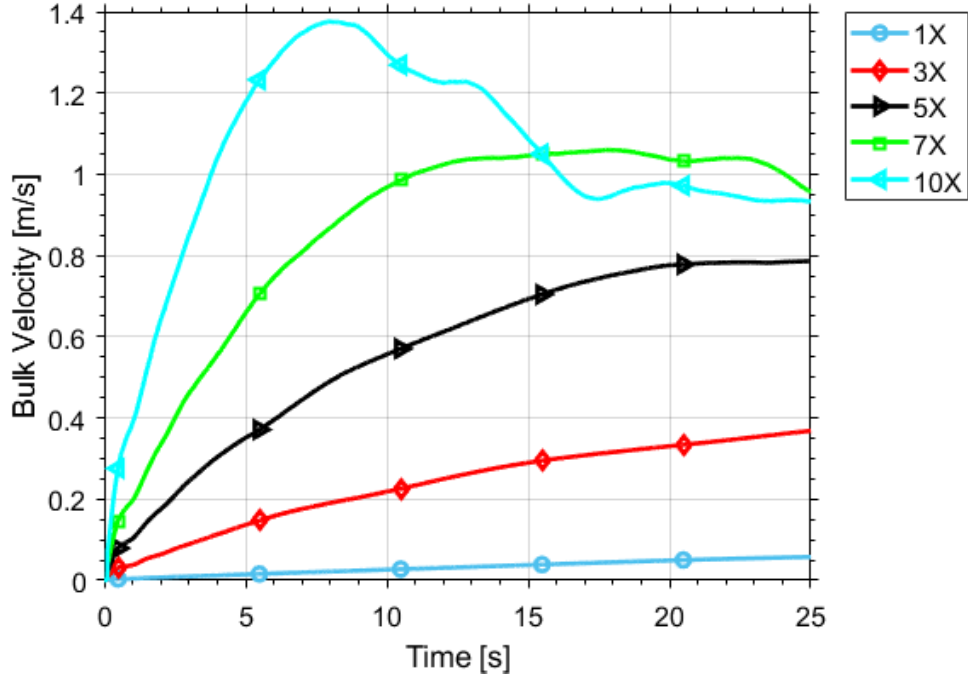
Fig. 4.11: MHD scaling factor analysis (I = 1500 [A]).

When $S_f = 1$, the velocity trend is linear resulting with a velocity under a magnitude of the expected value. This case had to run for over 120 seconds to obtain the proper velocity magnitude; however, the trend remained linear. This suggests that for any scaling factor the value will converge to the proper velocity value. For $S_f = 3$, the trend was between the expected curvature and the linear trend. The larger scaling

factors, 7 and 10, drastically increase in the first half then shoot down closer to the expected result. When $S_f = 5$, the development of the velocity trend was near the expected results, see Fig. (4.11). When the scaling factor was not large enough, the simulation accepted the false convergence which lead to nonphysical results, $S_f = 1$ or 3. When the factor was too large, $S_f = 7$ or 10, the velocity was overcome by the internal friction limit due to viscous forces; see the last paragraph of §2.3.4.

4.2.6 Flow Development

The literature study, [10], obtained a developed flow at 25 seconds of stirring. This study will be explored for case II rather than repeat the literature results for case I since the results for bulk velocity development and slag-eye formation matched closely with this study. This was accomplished by placing monitor points within the steel phase to track the velocity as the flow develops. Quasi-steady state was determined when the velocity profiles level out. Three planes were introduced into the steel phase, see Fig. (4.12a). Four points were set in each plane in a formation of an equilateral triangle, where 3 points were set at each vertex and one in the center, see Fig. (4.12b). This gave a total of twelve monitoring points within the steel phase, where the vertex points were at a distance of two-thirds the bottom radius.

(a) Flow monitor planes.

(b) Flow monitor vertex positioning.
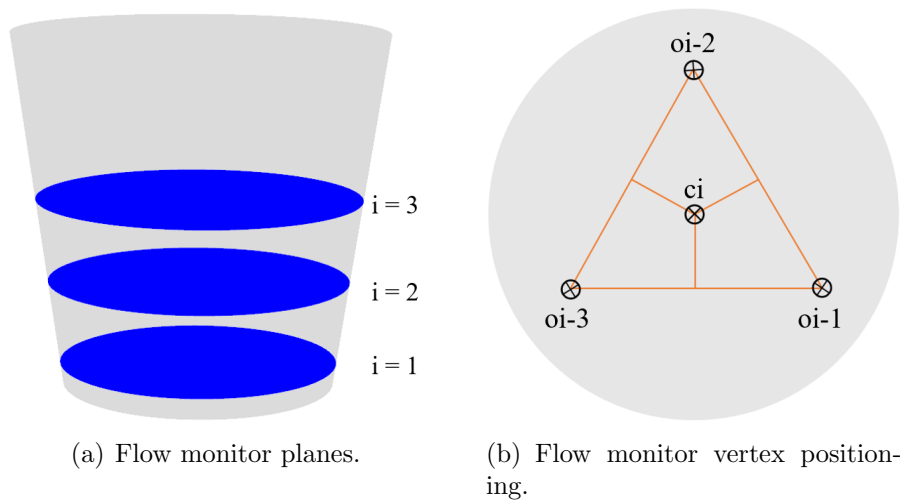
Fig. 4.12: Flow monitors.

The notation in Fig. (4.12b) has an **o** (outer point) for vertex point and a **c** (center point) for the center point and both are followed by an **i** (plane number). This was used to distinguish the points per plane and the position of each plane. Note that the vertex points were placed offset from the xy and zy planes.
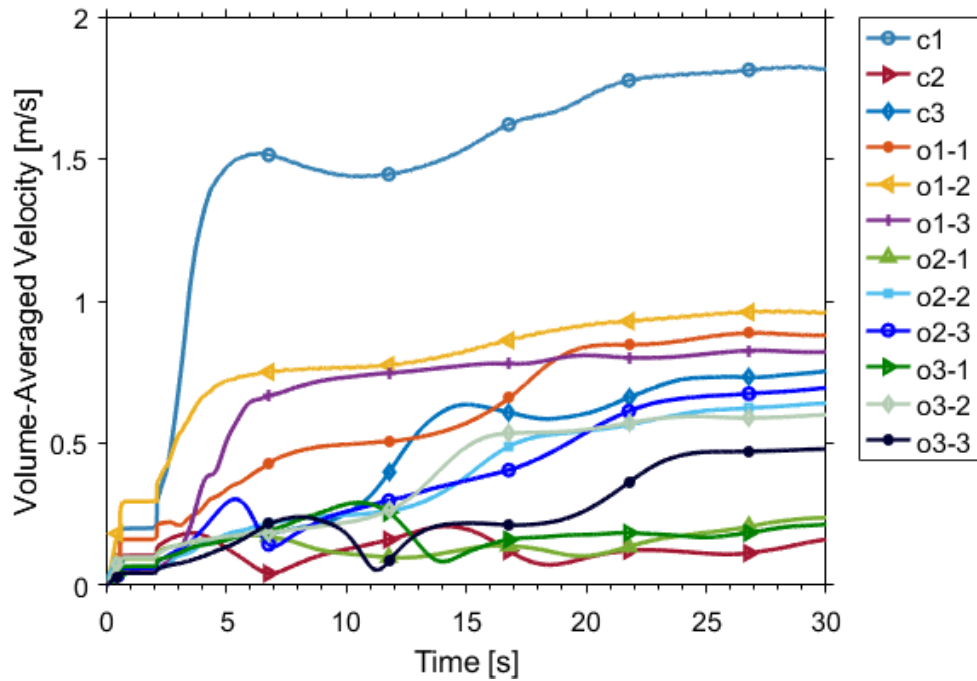
Fig. 4.13: Vertex point flow monitors.

The vertex averaged velocity data was obtained from these monitoring points. The evolution of these vertex velocities are shown in Fig. (4.13). From 25 to 30 seconds, the vertex velocities level off; therefore, quasi-steady state has been reached which closely matches the results obtained by the literature study, [10]. Note that the geometries and tonnage are different but the flow development is still comparable; therefore, it is expected that the development time would be similar.

The vertex point **c1** in Fig. (4.13) had a higher velocity profile over all other vertex points. This was caused by the high velocities near the bottom of the zy center plane. Plane 1 from Fig. (4.12a) was placed near the bottom to capture this high velocity region. All other vertex points were either positioned two-thirds the bottom radius

from the origin or in the horizontal planes above plane 1. In either case, they are away from the high velocity region. The outer points for plane 1 were in the vicinity of the left and right contour planes in Fig. (4.14), where the velocity was much lower.
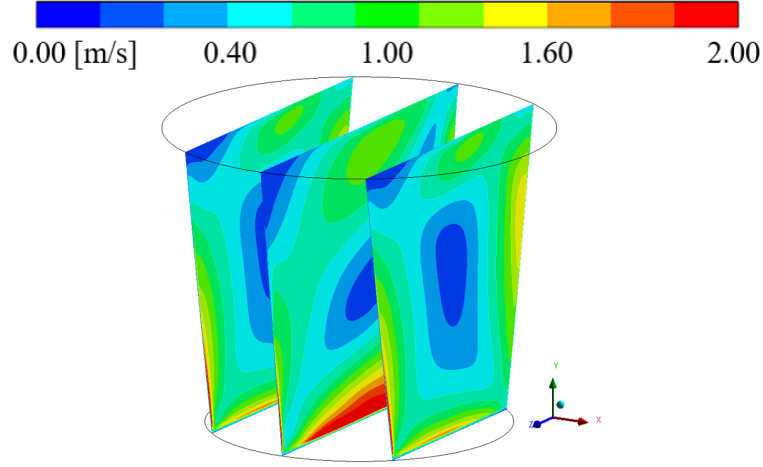
Fig. 4.14: Velocity contours on sample zy-planes.

4.2.7   Taper Angle Impact on the Slag-Eye Size and Bulk Velocity

The impact of the taper angle on the slag-eye formation and the bulk velocity has not been shown in previous literature studies ([3], [11], or [10]). This study was carried out with the geometry of case I at a constant amperage of 1500 [A]. The affect of the taper angle on the slag-eye was compared by an area ratio. This area ratio was calculated by evaluating the area of the slag-eye opening divided by the total cross-sectional area. The slag-eye comparison must be represented as an ratio since the diameter of the slag layer changes when the taper angle changes. The area was obtained by using a projected cross-section of the slag-eye.

Table 4.3: Taper angle impact on slag-eye at 1500 [A].

Taper Angle	Total Area [m^2]	Slag-Eye Area [m^2]	Area Ratio
0°	6.38	2.97	0.41
3°	7.50	2.87	0.38
5°	8.82	2.61	0.34

The results conclude that as the taper angle increases the velocity and slag-eye decrease, see Table (4.3) and Table (4.4). This occurs for two reasons: the taper angle increases the tonnage of the steel and the taper angle reduces the impact velocity at the slag-steel interface. An increase in tonnage creates a higher inertia for the stirrer to overcome, as evident in Table (4.4). Fig. (4.15a) shows that there is a higher velocity distribution than in Fig. (4.15b) on the wall opposite of the LF-EMS unit.

Table 4.4: Taper angle impact on velocity.

Angle [Degree]	Bulk Velocity [m/s]
0	0.79
3	0.72
5	0.69

(a) Taper angle: 0°. (b) Taper angle: 5°.
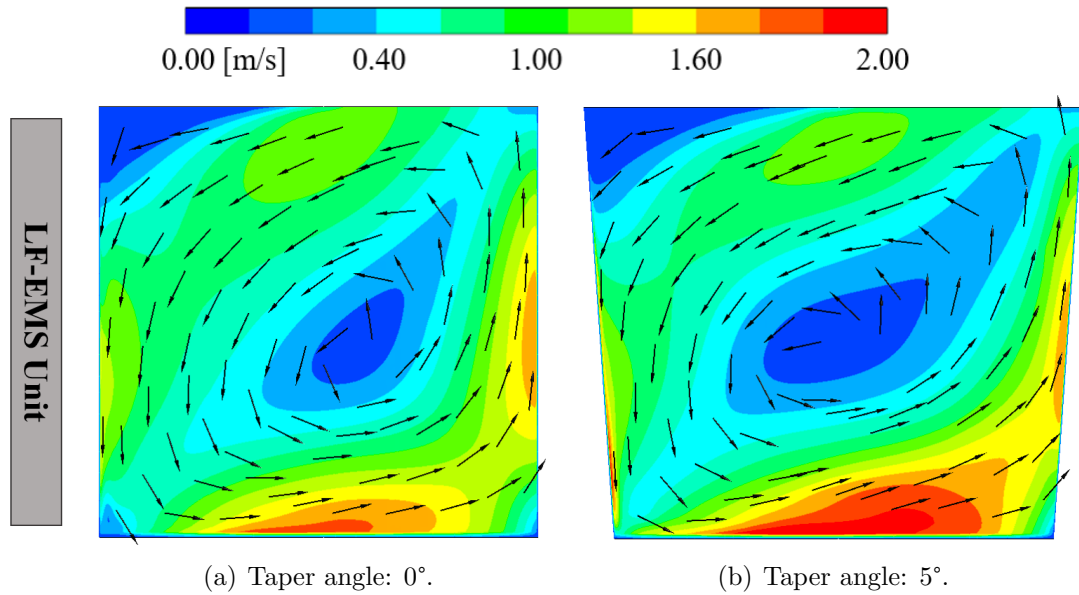
Fig. 4.15: ZY-plane contour of taper angle impact on velocity.

The velocity vectors in Fig. (4.15a) show that steel impacts the slag phase normal to the surface. This impact had maximum momentum impact which creates a larger slag-eye. The taper angle produces a longer side wall which allows the no-slip boundary condition to reduce to velocity. The perpendicular impact velocity is now reduced by a factor of the cosine of the taper angle, which reduces the momentum transfer

leading to a smaller slag-eye. In the case of the taper angle, the most prevalent inhibitor is the increase of tonnage.

(a) Taper angle: 0°.   (b) Taper angle: 5°.
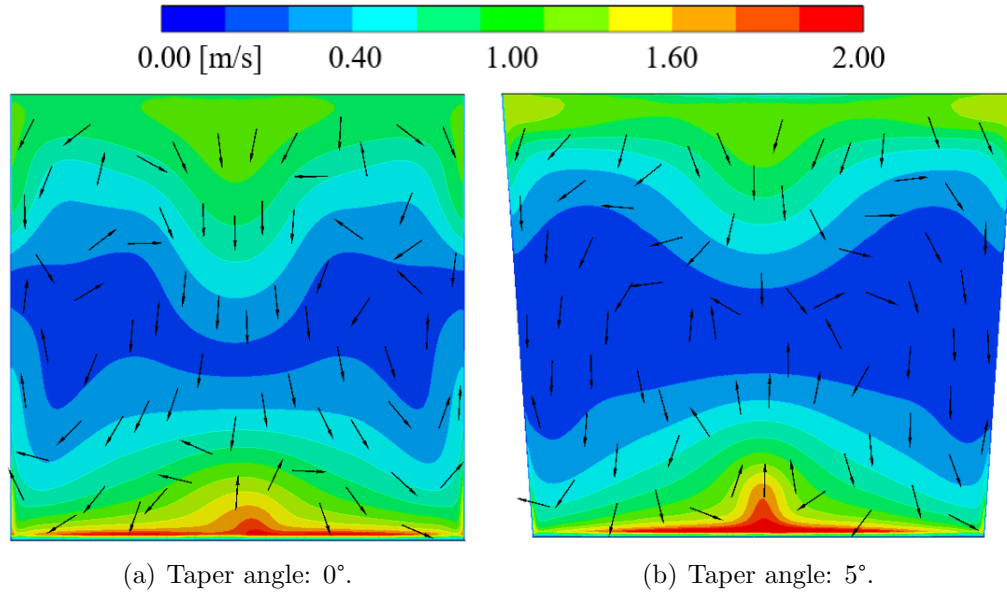
Fig. 4.16: XY-plane contour of taper angle impact on velocity.

A larger taper angle allows the vortex core to expand. The core is shown in Fig. (4.16a) and Fig. (4.16b) as the dark blue contour regions. The 5° taper angle vortex core is much larger than the cylindrical ladle. This accounts for a large portion of the bulk velocity for the 5° case. Momentum must be conserved therefore the velocity speeds up creating a high velocity region located near the bottom surface shown in Fig. (4.15b).

4.3   Comparison of Cases I and II

This study compares the geometry of case I and II with electric current values of 1200 and 1500 [A]. The bulk velocity was smaller in case II caused by the larger inertia as shown in Table (4.5). The velocity distributions in the xy and zy planes for case I and II at 1200 [A] are shown in Fig. (4.17) and Fig. (4.18). Fig. (4.17) slices the flow of the stirring direction. This shows that the two vortex plumes in

Fig. (4.10b) impact the flow far from the vortex core. Fig. (4.18) displays a similar feature; however, the vortex plumes are altered do to the taper angle. The vector field in this figure highlight the recirculation zones. The shape of the vortex core is also modified by the taper angle. This vortex core is stretched along the diagonal (left to right) of the xy-plane.

(a) XY-plane.　　　　　　　　　(b) ZY-plane.
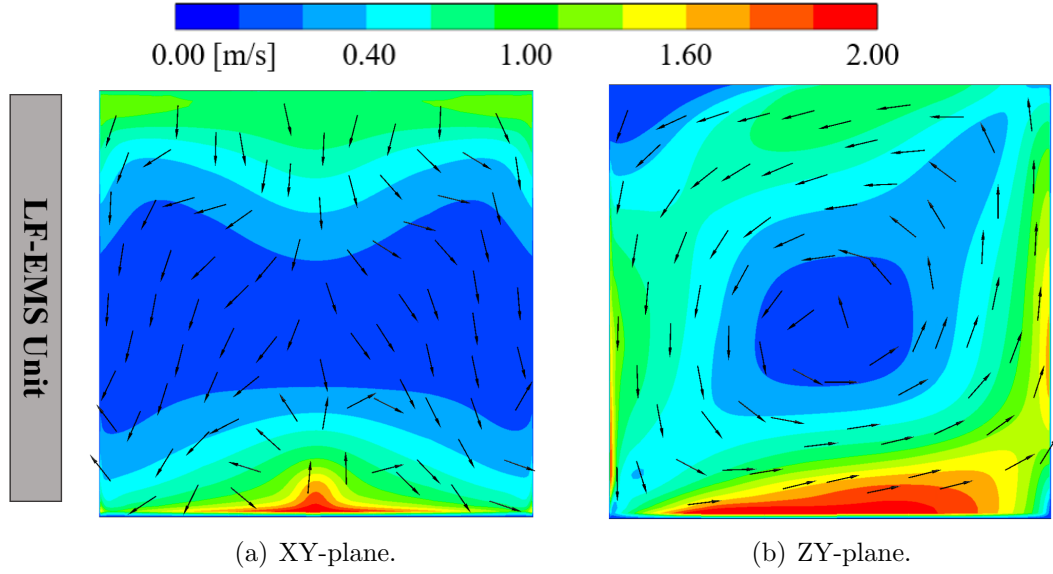
Fig. 4.17: Velocity contour and vector plot at 1200 [A] for case I.

(a) XY-plane.　　　　　　　　　(b) XY-plane.
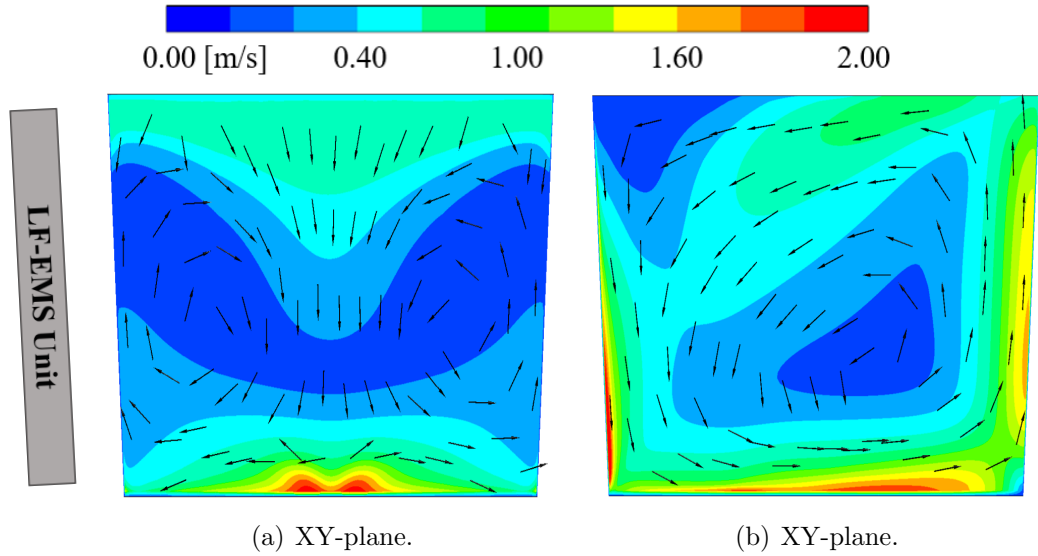
Fig. 4.18: Velocity contour and vector plot at 1200 [A] for case II.

4.3.1 Slag-Eye Formation

The slag-eye development was also compared between the geometries and current values. The lower current values produced smaller slag-eye openings, as shown earlier; however the effect of the taper angle and tonnage on the slag eye was larger than expected. The a comparison of the slag-eye area and developed bulk velocity is given in Table (4.5).

(a) Case I. (b) Case II.
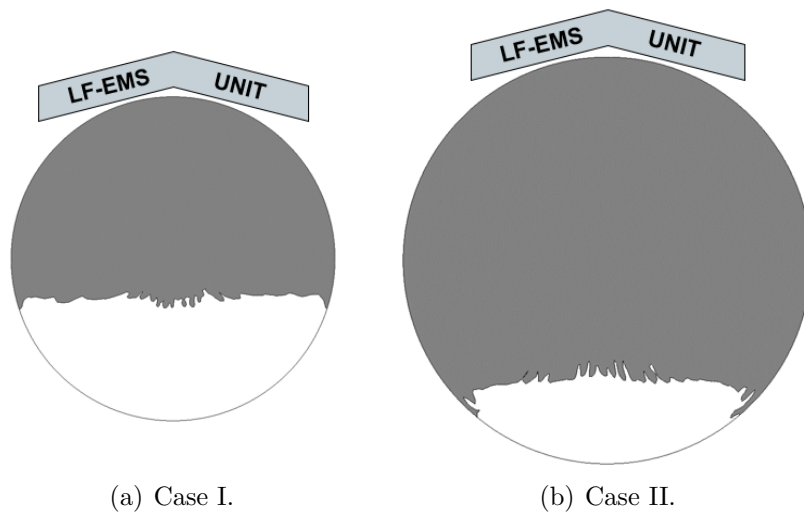
Fig. 4.19: Slag-eye at 25s for an amperage of 1200 [A].

(a) Case I. (b) Case II.
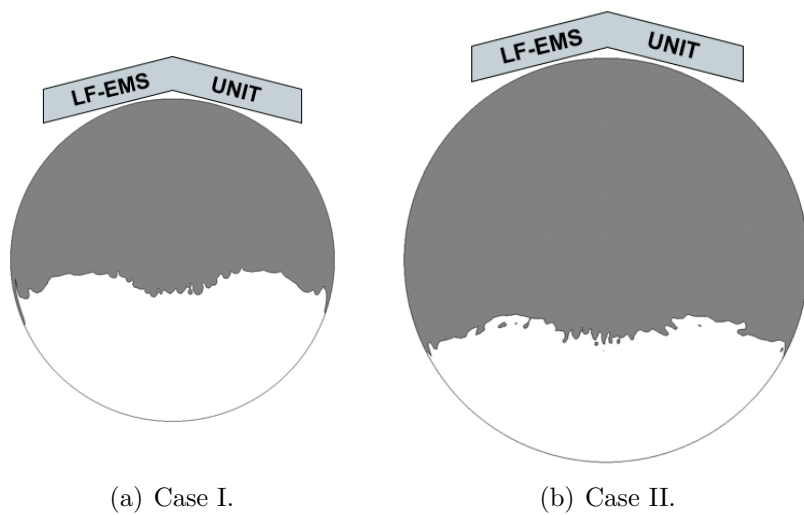
Fig. 4.20: Slag-eye at 25s for an amperage of 1500 [A].

64

Table 4.5: Geometry and amperage impact on velocity and slag eye.

Amperage [A]	Case	Velocity [m/s]	Eye Area [m²]	Area Ratio
1200	I	0.61	2.20	0.35
	II	0.50	1.40	0.14
1500	I	0.78	2.90	0.78
	II	0.66	2.75	0.66

4.3.2 Wall Shear Stress

Preventing ladle refractory wall depletion is a factor for ladle lifetime and safety. The stirring motion will wear the ladle wall away over time. Finding the areas of high erosion aids in predicting maintenance cycles. These high stress regions can be predicted through displaying the wall shear stress, see Fig. (4.21) and Fig. (4.22). An average of wall shear stress for a given amperage is provided in Table (4.6).

(a) Isometric view.

(b) Bottom (top of figure is near LF-EMS unit).
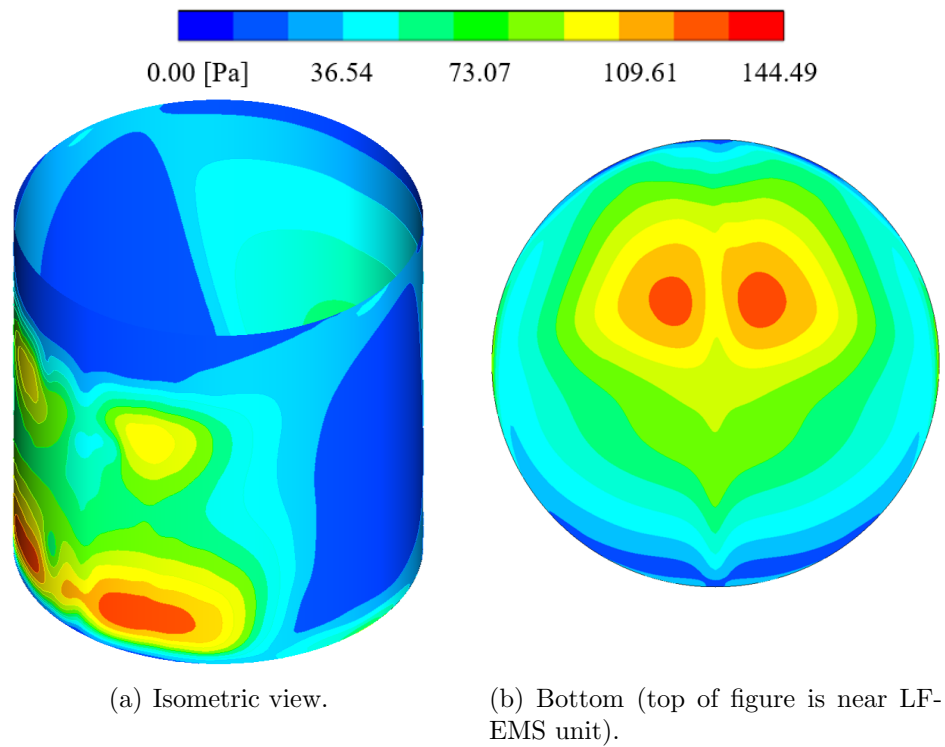
Fig. 4.21: Wall shear stress for case I at 1200 [A].

Table 4.6: Effect of amperage on average wall shear stress (case I).

Amperage [A]	Shear Stress [Pa]
1500	49
1350	45
1200	43
1050	42

In both cases the shear stress is highest at the bottom of the side and bottom wall near the LF-EMS unit. This is caused by the downward stirring forcing the fluid directly down into those regions with the two recirculating zones. Case II geometry showed that the vortex was distributed more throughout the melt. This is evident when comparing the minimum stress contours on the side walls as shown in Fig. (4.21a) and Fig. (4.22a). Case II has a much larger minimum stress contour on the sides since the vortex is more spread out; therefore creating less wear on the ladle side walls.

0.00 [Pa]   36.54   73.07   109.61   144.49

(a) Isometric view.

(b) Bottom (top of figure is near LF-EMS unit).
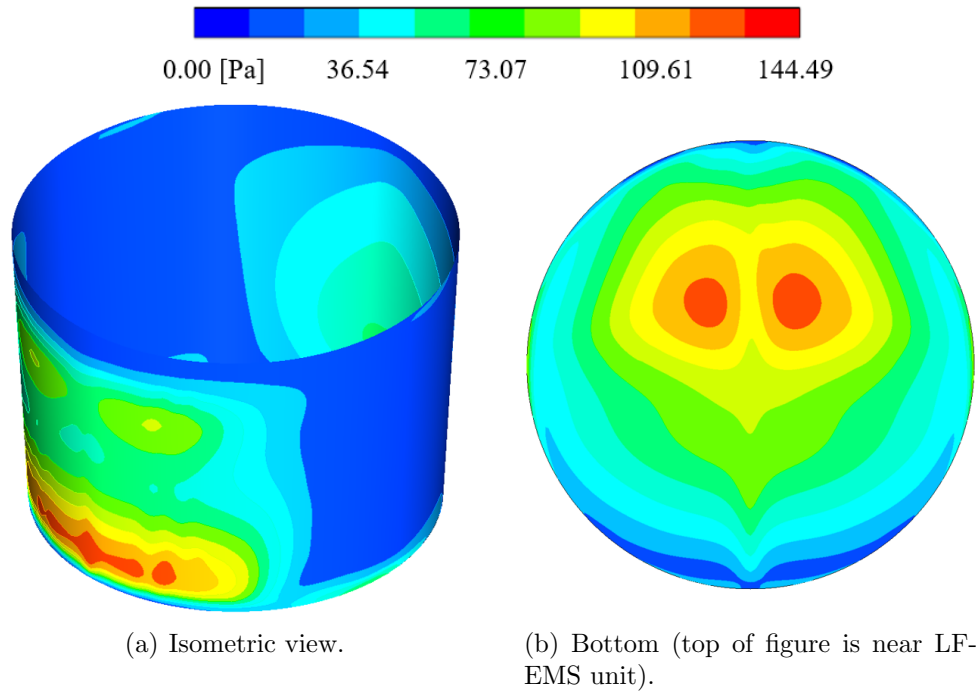
Fig. 4.22: Wall shear stress for case II at 1200 [A].

5. CONCLUSIONS AND RECOMMENDATIONS

5.1   Conclusions

This study developed an induction coil unit simulation to produce an external magnetic field along with a multiphase CFD simulation to study electromagnetic stirring within a metallurgical ladle. The LF-EMS unit simulation was utilized to produce various magnetic field strengths for studies on flow development, slag-eye formation, and the resulting wall shear stress. The FLUENT® MHD module scaling factor was explored and was found to be helpful in achieving results, and the scaling factor was determined to only be relevant within a small range where the maximum is constrained by internal friction. An MHD scaling factor of 5 was suitable for a TMF with a midrange magnitude of ~ 0.2 [T]. The developed bulk velocity was validated with a 0.98% difference with an absolute difference of 0.007 [m/s] against the literature study conducted by Sand et al 2009. The current work utilized the FLUENT® MHD module which under predicted for the majority of the flow evolution compared to the method used in the literature study. The parametric studies concluded that the taper angle has an inverse relation to velocity and slag-eye formation. The geometry study resulted in slag-eye reduction as the size increased. This was caused by the impact velocity on the slag interface to be smaller due to the innate higher inertia, and the taper angle altering the velocity impact angle. The wall shear stress was determined to distribute more in the larger ladle, as expected. The important takeaway is that the high shear stress regions were located on the floor and wall closest to the LF-EMS unit. These regions will be the cause of ladle wall erosion and potential breakouts.

5.2 Recommendations

5.2.1 Numerical Solver

A recommendation for the MHD solver is to use a multiphysics numerical solver such as STAR CMM+®, COMSOL Multiphysics®, or OpenFOAM®. The former two solvers have detailed tutorials which can greatly reduce to time spent troubleshooting and learning the solver package. The benefit of the multiphysics package is that there are no data transforms (the simulation is solved in a single domain).

5.2.2 Using the ANSYS FLUENT MHD Module Scaling Factor

The ANSYS FLUENT® MHD module, the scaling factor option is required for transient magnetic field. The MHD scaling factor has a strong correlation with the external magnetic field magnitude. This was tested against two other magnetic fields which were omitted from this study. A magnetic field with an average magnitude on the order of milliteslas required a scaling factor of ~ 25 where a field of centiteslas required a scaling factor of ~ 19. The field used in this simulation was on the order of deciteslas. The recommendation for properly implementing the scaling factor is to find the range at which viscous forces take control of the velocity limit. Once this is found the scaling factor can be fine tuned. The in-house code, with detailed comments, for formatting the magnetic field has been provided in **Appendix B**. If the magnetic field is simulated in ANSYS Electronics Desktop® then it is highly encouraged to use this code. If a future study requires the use of the Lorentz force distribution data then the user defined function (UDF) attached in **Appendix D** can be used. This UDF sets the force values as sources within the momentum equation to obtain a steady-state solution of the flow field.

5.2.3 Further Studies

A recommended study would be to determine whether inertia or taper angle have the larger effect on the slag eye formation. This can be done by using two additional geometries: a larger cylindrical ladle and the other the same tonnage with a taper angle. It would be an interesting study to dissect the amount of how much each partake in reducing the slag-eye opening.

The recommendation for combined EMGAS stirring would be to place an injection port between the high wall shear stress region on the floor as shown in Fig. (4.22b). A 90° dual port near the LF-EMS set up symmetrically about the zy-plane could also be used to breakup the high shear stress in this region. The only issue here would be for downward stirring, the flows would be opposing directions, which might result in overly gentle stirring. This should be explored with upward stirring.

5.3 Future Work

This CFD model is ready for the additional of the energy equation, combined EMGAS stirring, and inclusion removal. The thermal study of the EMS ladle will be very interesting for examining the energy dissipation caused by Joule heating. This can impact the flow distribution since some of the energy is lost to heat transfer. The combined EMGAS would be applicable for four reasons: insight to flow field development and stirring time, injection port positioning for reduction of wall shear stress, and determination of inclusion removal effectiveness. The inclusion removal in an EMS ladle is expected to be lower since it has less removal mechanism than the gas stirred ladle. Actually getting a quantitative analysis of this would be beneficial to industrial partners. These are all components of the future work of this project. This study sought to develop the models to explore the items listed. The inclusion removal and combined EMGAS models are currently being developed at CIVS. CIVS will further validate this model with industry provided data for the Lorentz force distribution.

REFERENCES

REFERENCES

[1] Q. Cao and L. Nastac, "Numerical modelling of the transport and removal of inclusions in an industrial gas-stirred ladle," *Ironmaking & Steelmaking*, vol. 45, no. 10, pp. 984–991, 2018.

[2] NSC, "An introduction to steelmaking," *New Steel Construction Archive*, 09 2017.

[3] M. Pal, "Modeling of induction stirred ladles," Ph.D. dissertation, Royal Institute of Technology, 06 2012.

[4] D. Mazumdar and R. Guthrie, "The physical and mathematical modelling of gas stirred ladle systems," *Isij International - ISIJ INT*, vol. 35, pp. 1–20, 01 1995.

[5] A. Thrum, "Induction or gas stirring in ladle furnaces – a comparison," *EEC, European Electric Steelmaking Conference*, vol. 2, no. 7, pp. 2–119, 7 2002.

[6] W. Lou and M. Zhu, "Numerical simulations of inclusion behavior in gas-stirred ladles," *Metallurgical and Materials Transactions B*, vol. 44, no. 3, pp. 762–782, Jun 2013.

[7] ABB Metallurgy, "Lf-ems reducing cost and improving quality," Brochure, 2014. [Online]. Available: https://library.e.abb.com/public/7fba886f58e74398bf45aa20b2ef6022/LF-EMS%20Broshure%20BSE044813_2.pdf

[8] E. Rousset and V. Fireteanu, "Simultaneous induction heating and electromagnetic stirring of a molten glass bath," 10 2015.

[9] P. A. Davidson, *Introduction to Magnetohydrodynamics*, 2nd ed., ser. Cambridge Texts in Applied Mathematics. Cambridge University Press, 2016.

[10] U. Sand, R. Bel Fdhila, H. Yang, and J.-E. Eriksson, "Control of gas bubbles and slag layer in a ladle furnace by electromagnetic stirring," 2009.

[11] M. Javurek, M. Barna, P. Gittler, K. Rockenschaub, and M. Lechner, "Casting and solidification flow modelling in continuous casting of round bloom strands with electromagnetic stirring," *Steel Research International*, vol. 79, 08 2008.

[12] D. J. Griffiths, *Introduction to electrodynamics; 4th ed.* Boston, MA: Pearson, 2013, re-published by Cambridge University Press in 2017.

[13] ANSYS Fluent, "Magnetohydrodynamics (mhd) module manual," 2003.

[14] F. Ulaby, *Electromagnetics for Engineers.* Pearson/Prentice Hall, 2005.

[15] J. Anderson, *Computational Fluid Dynamics: The Basics with Applications*, ser. McGraw-Hill International Editions: Mechanical Engineering.   McGraw-Hill, 1995.

[16] K. Dadzis, "Modeling of directional solidification of multicrystalline silicon in a traveling magnetic field," Ph.D. dissertation, 11 2012.

APPENDICES

A. DERIVATION OF THE MAGNETIC FIELD TRANSPORT EQUATION

The three governing equations for a magnetic field in MHD was covered in within §2.3.1. These equations are repeated here for ease of call back

$$\nabla \times \vec{E} = -\frac{\partial \vec{B}}{\partial t} \tag{A.1}$$

$$\nabla \times \vec{B} = \mu \vec{J} \tag{A.2}$$

$$\vec{J} = \sigma(\vec{E} + \vec{v} \times \vec{B}) \tag{A.3}$$

respectively. Rearranging Eq. (A.3) for $\vec{E}$ gives

$$\vec{E} = \frac{1}{\sigma}\vec{J} - (\vec{v} \times \vec{B}) \tag{A.4}$$

Solving for $\vec{J}$ in Eq. (A.2) gives

$$\vec{J} = \frac{1}{\mu}(\nabla \times \vec{B}) \tag{A.5}$$

Now, the expression from Eq. (A.5) can be substituted into Eq. (A.4) giving

$$\vec{E} = \frac{1}{\sigma\mu}(\nabla \times \vec{B}) - (\vec{v} \times \vec{B}) \tag{A.6}$$

Now implementing curl within the flux conservation of Faraday's law in Eq. (A.1) with Eq. (A.6) gives

$$\frac{\partial \vec{B}}{\partial t} = -\frac{1}{\sigma\mu}\underbrace{[\nabla \times (\nabla \times \vec{B})]}_{①} + \underbrace{\nabla \times (\vec{v} \times \vec{B})}_{②} \tag{A.7}$$

Now, ① can be simplified using the vector identity given [12] under the second derivatives section. This identity is

$$\nabla \times (\nabla \times \vec{A}) = \nabla(\nabla \cdot \vec{A}) - \nabla^2 \vec{A} \tag{A.8}$$

Applying this to Eq. (A.7) results in the final form of the transport equation

$$\boxed{\frac{\partial \vec{B}}{\partial t} = \nabla \times (\vec{v} \times \vec{B}) + \lambda \nabla^2 \vec{B}, \quad \lambda = \frac{1}{\mu \sigma}} \tag{A.9}$$

where λ is the magnetic diffusivity. Note, the first term in Eq. (A.8) drops out when applied to $\vec{B}$ due to the solenoidal nature of the magnetic field.

B. MAGNETIC FIELD EXPORT/IMPORT FORMATTING CODE

```matlab
1  clear; clc;
2  %===================================================================
3  %
4  %              ANSYS ELECTRONICS DESKTOP MAXWELL
5  %                  FIELD CALCULATOR EXPORT
6  %            CONVERSION TO ANSYS FLUENT IMPORT FORMAT
7  %
8  %                         REQUIREMENTS
9  %    - Export Fields (Real & Imaginary) from Maxwell (.fld)
10 %    - Run code and input the following information:
11 %         1. Name of Real magnetic field data file w/o ext.
12 %         2. Name of Imaginary magnetic field data file w/o ext.
13 %         3. Field Type (AC or DC)
14 %            3a. AC Field: enter frequency value then press enter
15 %            3b. DC field: press enter
16 %
17 %    N.B. Only tested with 2D & 3D real and imaginary values
18 %    N.B. Use the same spatial units for all export items
19 %         when exporting in the Maxwell Electronics
20 %         Desktop Field Calculator
21 %         ---------------------------------
22 %         | created by:                   |
23 %         |           Joshua D. Vandenoever |
24 %         |-------------------------------|
25 %
26 %===================================================================
27
28 %===================================================================
29 %              USER INPUT FOR EXPORTED MAXWELL FILES
30 %===================================================================
31
32 real_b_data_file = strcat(input...
33    ('Input the REAL B field data file exported: \n','s'),'.fld')
         ;
34 imaginary_b_data_file = strcat(input...
35    ('\nInput the IMAGINARY B field data file exported: \n','s'),
         '.fld');
36
37 % Rename (Optional)
38 exportFileName = 'B_Data_for_Fluent_MHD_Module.txt';
39
40 %===================================================================
```

```
41  % EXTRACT UNITS & SPACING VALUES FROM MAXWELL EXPORT CALCULATOR
42  %=============================================================
43
44  % Extract headers (1st row)
45  fid = fopen(real_b_data_file);
46  info = strsplit(fgetl(fid), ' ');
47  fclose(fid);
48
49  % Extract units used to export field values in Maxwell
50  unit = char(info{4});
51  unit = strip(unit,'[');
52  unit = unit(end-1:end);
53
54  % Extract x spacing used in Maxwell
55  x_space = char(info{13});
56  x_space = strip(x_space,'[');
57  x_space = str2double(x_space(1:end-2));
58
59  % Extract y spacing used in Maxwell
60  y_space = char(info{14});
61  y_space = str2double(y_space(1:end-2));
62
63  % Extract z spacing used in Maxwell
64  z_space = char(info{15});
65  z_space = strip(z_space,']');
66  z_space = str2double(z_space(1:end-2));
67
68  %=============================================================
69  % USER INPUT: FREQUENCY TYPE & VALUE USED IN MAXWELL SIMULATION
70  %=============================================================
71
72  % Conversion between units
73  % (Note, if you are using some weird unit then edit the code)
74  if strcmp(unit, 'mm') == 1
75      m = 1000;
76  elseif strcmp(unit, 'cm') == 1
77      m = 100;
78  else
79      m = 1; % Default is in meters ('m')
80  end
81
82  % User input for frequency
83  type = input('\nDC or AC FIELD (Enter DC or AC):\n','s');
84  if strcmp(type,'DC') == 1 || strcmp(type,'dc') == 1
85      field = 0;
86      freq = 0;
87  elseif strcmp(type,'AC') == 1 || strcmp(type,'ac') == 1
88      field = 1;
89      freq = input('\nEnter frequency in [Hz]:\n');
90  else
91      disp('You entered in something wrong')
92  end
93
```

```matlab
94  %==========================================================================
95  %                          EXTRACTING & SORTING DATA
96  %==========================================================================
97
98  % Read data starting from the second row
99  real_B_data = dlmread(real_b_data_file,' ', 2,0);
100 imaginary_B_data = dlmread(imaginary_b_data_file,' ', 2,0);
101
102 % Create array consisting of coordinates (firt 3 cols),
103 % real B (next three), and imaginary B (last three cols)
104
105 % Extract geometry values from file
106 % for i = 1:3
107 %     geo_b(:,i) = real_B_data(:,i);
108 % end
109 %
110 % % Note, Matlab import adds a col of zeros (col:4)
111 %
112 % % Extract real B values from file
113 % for i = 4:6
114 %     geo_b(:,i) = real_B_data(:,i+1);
115 % end
116 %
117 % % Extract imaginary B values from file
118 % for i = 7:9
119 %     geo_b(:,i) = imaginary_B_data(:,i-2);
120 % end
121
122 %
123 geo_b(:,1) = real_B_data(:,1);% Extract geometry values from file
124 geo_b(:,2) = real_B_data(:,2);
125 geo_b(:,3) = real_B_data(:,3);
126 geo_b(:,4) = real_B_data(:,5);% Extract real B values from file
127 geo_b(:,5) = real_B_data(:,6);% Note, Matlab import adds a col of
        zeros (col:4)
128 geo_b(:,6) = real_B_data(:,7);
129 geo_b(:,7) = imaginary_B_data(:,5);% Extract imaginary B values
        from file
130 geo_b(:,8) = imaginary_B_data(:,6);
131 geo_b(:,9) = imaginary_B_data(:,7);
132 %
133
134 % Sort data based on Z,Y,X positions
135 sorted_data = sortrows(geo_b,[3,2,1]);
136
137 % Extract only field data from sorted data
138 % for i = 1:6
139 %     b_sorted(:,i) = geo_b(:,i+3);
140 % end
141
142 %
```

```matlab
143  b_sorted(:,1) = sorted_data(:,4);
144  b_sorted(:,2) = sorted_data(:,5);
145  b_sorted(:,3) = sorted_data(:,6);
146  b_sorted(:,4) = sorted_data(:,7);
147  b_sorted(:,5) = sorted_data(:,8);
148  b_sorted(:,6) = sorted_data(:,9);
149  %
150
151  %=================================================================
152  %                    TEXT FILE HEADER INFORMATION
153  %=================================================================
154
155  % Line 1
156  header_line_1 = 'MAG-DATA';
157
158  % Line 2 | Used to calculate nX, nY, nZ (in original units)
159  nX = ((max(geo_b(:,1))*m - min(geo_b(:,1))*m))/x_space + 1;
160  nY = ((max(geo_b(:,2))*m - min(geo_b(:,2))*m))/y_space + 1;
161  nZ = ((max(geo_b(:,3))*m - min(geo_b(:,3))*m))/z_space + 1;
162
163  % Lines 3-5 | Obtained from above code
164  % Line 6 | Obtained from user input
165
166  %=================================================================
167  %                 FORMATTING & EXPORTING TEXT FILE
168  %=================================================================
169
170  fileID = fopen(exportFileName,'w'); % file name for fluent import
171  fprintf(fileID,'%s\r\n',header_line_1);
172  fprintf(fileID,'%.0f\t %.0f\t %.0f\r\n', nX, nY, nZ);
173  fprintf(fileID,'%.2f\t %.2f\r\n',min(geo_b(:,1)), max(geo_b(:,1))
       );
174  fprintf(fileID,'%.2f\t %.2f\r\n',min(geo_b(:,2)), max(geo_b(:,2))
       );
175  fprintf(fileID,'%.2f\t %.2f\r\n',min(geo_b(:,3)), max(geo_b(:,3))
       );
176  fprintf(fileID,'%.0f\t %.2f\r\n', field, freq);
177  fprintf(fileID,'%0.2E\t %0.2E\t %0.2E\t %0.2E\t %0.2E\t %0.2E\r\n
       ',b_sorted');
178  fclose(fileID);
179
180  %=================================================================
181  %                          END OF CODE
182  %=================================================================
183
184  % Have fun finding the data file
185  fprintf('\nNote: data file should be in current working directory
        named:\n\t%s\n',exportFileName)
```

C. QUARTER-WAVELENGTH AVERAGING OF AN OSCILLATING PROFILE

This code was created for two purposes: post-processing the oscillating data and providing consistent plots. As mentioned in §4.2.1, the raw data had minuscule oscillations during the velocity development. The post-processing scheme, shown in the code below, was developed after observing that the amplitudes of the oscillations were negligible. The code works on the principle of quarter-wavelength averaging. For data points that are within a full wavelength, a given data point is averaged with two data values each quarter-wavelength on either side of the given point. An example is depicted in Fig. (C.1) where the orange dashed line is the post-processed profile. For data points that are not included in a full wavelength (i.e. the beginning or end of a oscillating profile) only has access to half-wavelength of data, therefore this situation cannot be post-processed in the same manner. The averaging for a given data point in this predicament is achieved by averaging the given data point with a successive (beginning oscillation) or recessive (ending oscillation) point that is a half-wavelength away from the given data point.
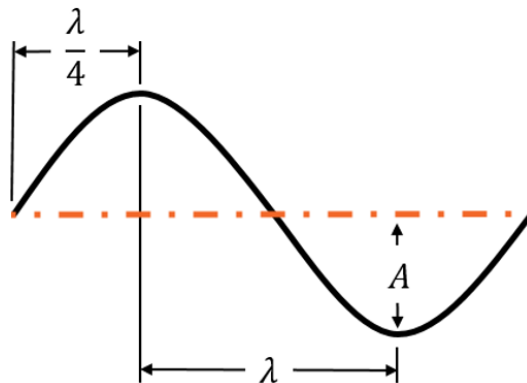
Fig. C.1: Wavelength and amplitude of an oscillation (black profile). The dashed orange line indicates the average of the oscillation.

```matlab
clear;clc;
%=======================================================================
%
%                        OSCILLATING  PROFILE
%                     QUARTER-WAVELENGTH  AVERAGING
%
% 1. PURPOSE:
%       This  code  will  average  an  oscillating
%       data  set  to  obtain  a  smooth  curve.
%
% 2. REQUIREMENTS (*optional):
%       - Determine  wavelength  of  oscillations
%       - Data  formatting  in  Excel  file:
%           1. First  profile  data  in  first  sheet  and  so  forth
%             - col A (x):  consistent  data (e.g.  time)
%             - col B (Y):  oscillating  data (e.g.  velocity)
%             - row 1 (X & Y):  header  rows (e.g.  t & vel)
%             - Keep  consistent  formatting  per  sheet (first 2 cols)
%             - All  sheets  for  profiles  must  be  successive
%             - *Add  comparison  profile  to  last  sheet  in  Excel  file
%           2. Set  the  following  items (Section 1: User Input)
%             - File  name (Line: )
%             - Plot  image  filename  w/o  extension (Line: )
%             - Number  of  profiles  to  be  plotted (Line: )
%             - Number  of  rows (Line: )
%             - Quarter-wavelength 'interval' (Line: )
%             - *Excel  sheet  number  which  contains  comparison  data
%                 - Set  Line = 0  for  no  comparison  profile
%             - Titles:  Lines:
%             - Plot  ranges (Lines: )
%             - Legend  titles:  Lines:
%
% 3. Notes:
%       - Quarter-wavelength (interval)  must  be  an  integer
%       - Limited  to  15  profiles
%           1. For  more  plots  extend:
%             - Legend  Titles (Line: )
%             - RGB  color  vectors (Lines: )
%       - *Enable:
%           1. Sanity  Check - Uncomment (Lines: )
%           2. Plot  Title - Uncomment (Line: )
%           3. Guide  Lines - Uncomment (Line: )
%
%                   ---------------------------------
%                   |                               |
%                   | created  by:  Joshua D. Vandenoever |
%                   | ------------------------------- |
%
%=======================================================================
```

```matlab
51  %============================================================================
52  % Section 1                         USER INPUT
53  %============================================================================
54
55  file = 'excel_file_raw_data.xlsx'; % xlsx name w/ext.
56  save_plot_as = 'plot_post_processed';
57  profile_count = 3; % Number of profiles to be graphed
58                     % This also defines the number of xlsx sheets
59  % Set range for xlsx reader
60  row_count = 3000; % Number of rows (data range)
61  nrows = num2str(row_count); % Set xlsx range as str
62  x_xlsx = strcat('A2:A',nrows); % 2: 2nd row (skip header)
63  y_xlsx = strcat('B2:B',nrows);
64
65  wavelength = 0.48;
66  x_increment = 0.01; % Increment of consistent data
67  interval = round(0.25*wavelength/x_increment,0);
68  % Position where oscillations develop
69  oscillation_start = 100;
70
71  % Comparison profile data (Input 0 for no comparison)
72  compare_sheet = 0; % Sheet number for comparison profile
73  if compare_sheet == 0
74      % Zero means no comparison plot
75  else
76      compare_x = xlsread(file ,compare_sheet ,x_xlsx);
77      compare_y = xlsread(file ,compare_sheet ,y_xlsx);
78  end
79  %----------------------------------------------------------------------------
80  %     Plot Details
81  %----------------------------------------------------------------------------
82
83  % Titles
84  chart_title = 'TITLE'; % Uncomment (Line: )
85  xaxis = 'X-AXIS'; % Use {'Long title';'title next line'} for long
86  yaxis = 'Y-AXIS'; % titles
87
88  % Chart Limits
89  x_range = [0 25]; % [x_o x_f]
90  y_range = [0 0.8]; % [y_o y_f]
91
92  post_profile_thickness = 2; % Thickness of graphed line
93  raw_profile_thickness = 1.25; % Thickness of graphed line
94
95  % Legend titles | note: leave one space before the title
96  legend_titles = [" legend_1",...
97                   " legend_2",...
98                   " legend_3",...
99                   " legend_4",...
100                  " legend_5",...
101                  "","","","","","","","","",""];
102
103 plot_symbol = ["-o",...
```

```
104                        "−d " ,...
105                        " − >",...
106                        "−s " ,...
107                        " − ∗",...
108                        "−h","−x"," − ^", "−s", "−p"];
109
110  mark_space = round ((x_range(2)/x_increment)/5,0); % Space between
         markers on profile
111  mark_size = 7; % Default size of profile marker
112  plt_sym_i = 1; % Count symbol to loop for larger datasets
113
114  legend_location = 'best'; % or use 'bestoutside'
115
116  %=====================================================================
117  % Section 2               SET COLORS FOR PROFILES
118  %=====================================================================
119
120  % RGB color schemes
121   r = [0.301  1.000  0.466  1.000  0.000...
122         0.494  0.635  0.000  0.850  0.929...
123         0.494  0.466  0.301  0.000  0.000];
124   g = [0.754  0.000  0.674  0.500  0.184...
125         0.750  0.078  0.447  0.325  0.694...
126         0.184  0.674  0.745  0.000  0.500];
127   b = [0.933  0.000  0.188  0.000  0.556...
128         0.250  0.250  0.184  0.741  0.098...
129         0.125  0.556  0.188  0.933  1.000];
130
131  %=====================================================================
132  % Section 3               SANITY CHECK
133  %=====================================================================
134
135  % check = input('Run sanity check? (Type: y or n) ','s');
136  % if check == 'y'
137  %     for c = 1:profile_count % Display header (A1:A1) per sheet
138  %       [~,txtData] = xlsread(file,c,'A1:A1')
139  %     end
140  %     pause(5) % Check printout before continuing
141  % end
142
143  %=====================================================================
144  % Section 4                      PLOTTER
145  %=====================================================================
146
147  figure hold on
148  for c = 1:profile_count
149      fprintf('Post−Processing Profile: %d\n',c)
150      x_post = []; % Re−initialize
151      y_post = [];
152      x_raw=xlsread(file,c,x_xlsx);
153      y_raw=xlsread(file,c,y_xlsx);
154
155      for i = 1:oscillation_start % Ignore post−processing unitl
```

```matlab
156                y_post(i) = y_raw(i);   % ocsillations start
157        end
158
159        %————————————————————————————————————————————
160        %       Quarter−Wavelength Interval Averaging
161        %————————————————————————————————————————————
162
163        for  i = oscillation_start:length(y_raw)
164            if  i <= interval
165                y_post(i) = (y_raw(i)+y_raw(i+2*interval))/2;
166            elseif  i >= interval && i <= length(y_raw)−interval
167                y_post(i) = (y_raw(i+interval) + y_raw(i−interval))
                        /2;
168            else
169                y_post(i) = (y_raw(i)+y_raw(i−2*interval))/2;
170            end
171        end
172
173        x_post = x_raw; % Consistent data
174
175        %————————————————————————————————————————————
176        %       Plot  Commands
177        %————————————————————————————————————————————
178
179        % Alter  specific  plot  symbol  size  for  aesthetics
180        if  plot_symbol(plt_sym_i) == "−s"
181            marker_size = 9;
182        else
183            marker_size = mark_size;
184        end
185
186        plot(x_post, y_post,...
187            plot_symbol(plt_sym_i),...
188            'MarkerIndices',...
189            mark_space:mark_space:length(x_post)−mark_space,...
190            'MarkerSize',marker_size,...
191            'Color', [r(c) g(c) b(c)],...
192            'linewidth',post_profile_thickness,...
193            'DisplayName',legend_titles(c));
194
195        % Reset  plot  symbol  count  at  end  of  symbol  list
196        if  plt_sym_i == length(plot_symbol)
197            plt_sym_i = 1;
198        end
199        % Update  symbol  position
200        plt_sym_i = plt_sym_i + 1;
201
202        %————————————————————————————————————————————
203        %       Plot Raw Data Along w/ Post−Processed Profiles
204        %————————————————————————————————————————————
205
206        % Plot  raw  data  along  with  post−processed  data
207 %      hold  on  % Required!
```

```matlab
208 %        plot(x_raw, y_raw, '-',...
209 %           'Color', [r(c) g(c) b(c)],...
210 %           'linewidth',raw_profile_thickness,...
211 %           'HandleVisibility','off')
212
213     % End of post-processing
214     if c == profile_count
215         disp('Complete (plot saved as png)')
216     end
217 end
218
219 %==============================================================
220 % Section 5        ADD COMPARISON PROFILE TO PLOT
221 %==============================================================
222
223 if compare_sheet == 0
224     % Zero means no comparison plot
225 else
226     plot(compare_x, compare_y, '--',...
227         'DisplayName', " Comparison",...
228         'color','k','linewidth',post_profile_thickness);
229 end
230
231 %==============================================================
232 % Section 6        ADD GUIDE LINES(S) TO PLOT
233 %==============================================================
234
235 % Line coords: ([x_o x_f], [y_o y_f])
236 % plot([10 10], [0 0.8], '--', ...
237 %     'Color',[0 0 0],'linewidth',2,...
238 %     'DisplayName'," 0% Error")
239
240 %==============================================================
241 % Section 7                LEGEND SPECIFICS
242 %==============================================================
243
244 [lgnd] = legend('show','location',legend_location);
245     set(lgnd,'FontSize',12); % Set legend font size
246     % Change legend 'token' (color line) size (default: [30,18])
247     lgnd.ItemTokenSize = [24,15]; % Legend line size
248     set(gca,'FontSize',12)% Set font size of axes numbers
249 %     title(chart_title,'FontSize',14); % commented for paper use
250     xlabel(xaxis,'FontSize',11)% Axis labels
251     ylabel(yaxis,'FontSize',11)
252     xlim(x_range); % Horizonal range
253     ylim(y_range); % Vertical range
254
255 set(gca, ...
256         'Box'          , 'on'       , ...
257         'TickDir'      , 'out'      , ...
258         'TickLength'   , [.01 .01]  , ...
259         'XMinorTick'   , 'on'       , ...
260         'YMinorTick'   , 'on'       , ...
```

```matlab
261          'XGrid'          ,  'on'          ,  ...
262          'YGrid'          ,  'on'          ,  ...
263          'XMinorGrid'     ,  'off'         ,  ...
264          'YMinorGrid'     ,  'off'         ,  ...
265          'XColor'         ,  [0  0  0]     ,  ...
266          'YColor'         ,  [0  0  0]     );
267
268  saveas(gcf,  save_plot_as,  'png')
269  %===============================================================
270  %                        END OF CODE
271  %===============================================================
```

D. ANSYS FLUENT USER-DEFINED FUNCTION FOR IMPORTING LORENTZ FORCE DENSITY DATA

This UDF readings in a data file containing Cartesian coordinate data with corresponding Lorentz force components. The first line of the data file is set for the count of rows for the data set. A data row is formatted as:

Column Index	Data Contained
1	X
2	Y
3	Z
4	F_X
5	F_Y
6	F_Z

This will read the data from the file and store the coordinates and force values as user-defined memory within FLUENT. The Lorentz force values will be used as momentum source terms. This code is purposed to allow for a steady-state solution to be obtained without solving the MHD equations when a proper data set is available. This code has not been tested but was attached to help other researchers by providing a steppingstone for working with MHD in FLUENT®.

```
 1  /* UDF: Set Lorentz Force Distribution Values as Momentum Source
        Terms  */
 2  /*        -------------------------------
 3            | created by:                   |
 4            |         Joshua Vandenoever    |
 5            | ----------------------------- |
 6  */
 7  #include "udf.h"
 8  #include "mem.h"
 9
10  #define POINTS 1000000 /* Large value used to initialize size of
        col vectors */
11  #define SteelID 0 /* Zone ID (Primary: 0)*/
```

```c
12
13 static float X[POINTS], Y[POINTS], Z[POINTS], XF[POINTS], YF[
       POINTS], ZF[POINTS];
14 static int COUNT; /* Used for number of rows */
15
16 int numberMatched = 0; /* Count for matched coordinates */
17
18 DEFINE_ON_DEMAND(ForceDensityArray)
19 {
20 int i;
21 float coord[ND_ND];
22 float tol=0.00001; /* Tolerance betweeen data coordinates and
       FLUENT mesh coords */
23 static int init = 0; /* "Stopping criterion" */
24
25 FILE *fp;
26 fp = fopen ("force.txt", "r");
27 fscanf(fp,"%d", &COUNT); /* Get number of rows from 1st row of
       data file */
28
29 for (i=0;i<COUNT;i++) /* read in coords and force values into col
        vectors */
30 {
31          fscanf(fp,"%f %f %f %f %f %f", &X[i], &Y[i], &Z[i], &XF[i
                ], &YF[i], &ZF[i]);
32 }
33 fclose(fp);
34
35 /* Printout to FLUENT console that data was read and how many
       rows in data set (Sanity Check)*/
36 #if !RP_NODE
37 Message("\n");
38 Message("count: %d\n",COUNT);
39 Message("data loaded...\n");
40 #endif
41
42 if (init == 0) /* Ensures only one loop through all the threads
       */
43 {
44 Domain *d = Get_Domain(1);/*1 is highest level (mixture)*/
45 Thread *t;
46 cell_t c;
47 thread_loop_c(t,d)          {
48 Thread *t_steel = THREAD_SUB_THREAD(t, SteelID);
49 begin_c_loop(c,t_steel)
50 {
51 C_UDMI(c,t_steel,0) = 0.; /* Initialize all to zero */
52 C_UDMI(c,t_steel,1) = 0.;
53 C_UDMI(c,t_steel,2) = 0.;
54 C_CENTROID(coord,c,t_steel);
55 for (i=0;i<COUNT;i++)
56 {
```

```
57  if (fabs(coord[0]-X[i]) < tol  && fabs(coord[1]-Y[i]) < tol &&
        fabs(coord[2]-Z[i]) < tol)
58  {
59  C_UDMI(c,t_steel,0)=XF[i];
60  C_UDMI(c,t_steel,1)=YF[i];
61  C_UDMI(c,t_steel,2)=ZF[i];
62  //Message("match found: %d (X: %f, Y: %f, Z: %f)\n",i,X[i], Y[i],
        Z[i]);  /* (Sanity Check) */
63  numberMatched += 1;
64  }
65  }
66  }
67  end_c_loop(c,t)
68  }
69  init = 1;
70  }
71  Message("Total matched: %d\n", numberMatched); /* Output will
        show per thread (# processors) used */
72  }
73
74  DEFINE_SOURCE(source_x, c, t, dS, eqn)
75  {
76  real force;
77  Thread *tmixture = THREAD_SUPER_THREAD(t);
78
79  force = C_UDMI(c,t,0)/C_VOLUME(c,t); /* Units: [N/m^3] */
80
81  dS[eqn] = 0;
82  return force;
83  }
84
85  DEFINE_SOURCE(source_y, c, t, dS, eqn)
86  {
87  real force;
88  Thread *tmixture = THREAD_SUPER_THREAD(t);
89
90  force = C_UDMI(c,t,1)/C_VOLUME(c,t); /* Units: [N/m^3] */
91
92  dS[eqn] = 0;
93  return force;
94  }
95
96  DEFINE_SOURCE(source_z, c, t, dS, eqn)
97  {
98  real force;
99  Thread *tmixture = THREAD_SUPER_THREAD(t);
100
101 force = C_UDMI(c,t,2)/C_VOLUME(c,t); /* Units: [N/m^3] */
102
103 dS[eqn] = 0;
104 return force;
105 }
```